This document is the accepted manuscript version of the following article:
Marchetti, G., Manconi, A., & Comiti, F. (2023). Limitations in the use of Sentinel-1 data for morphological change detection in rivers. International Journal of Remote Sensing, 44(21), 6642-6669. https://doi.org/10.1080/01431161.2023.2274317

Limitations in the use of Sentinel-1 data for morphological change detection in rivers

Marchetti Giulia[a,b*], Manconi Andrea [c], Comiti Francesco[a]

[a]Faculty of Science and Technology, Free University of Bozen, Bolzano-Bozen, Italy; [b]Italian Institute for Environmental Research and Protection (ISPRA), Rome, Italy; [c]Climate Change, Extremes and Natural Hazards in Alpine Regions Research Centre CERC, WSL Institute for Snow and Avalanche Research SLF

*giulia.marchetti@isprambiente.it

Limitations in the use of Sentinel-1 data for morphological change detection in rivers

The identification of morphological changes occurring along river channels is essential to support river process understanding, assess sediment budgets and evaluate the effectiveness of river management. Among available remote sensing techniques, space-borne synthetic aperture radar (SAR) could potentially provide a powerful complement to optical imagery for this task. However, very few studies have been carried out on the use of SAR datasets to study erosion and deposition processes in river channels. In this work, we investigate the potential of change detection analysis based on Sentinel-1 data, by comparing variations of radar backscattering to river morphology changes identified through high-resolution drone acquisitions. We considered a time series of two years of Sentinel-1 data relative to a period where, despite a moderate fluvial event occurred, morphological changes have been significantly detected in multitemporal drone point clouds. Satellite optical imagery (planet.com) and hydro-meteorological data were used to support the analysis and interpret results. The results show that the spatial and temporal resolution of Sentinel-1 is currently not suitable for accurate discrimination of morphological changes related to river dynamics at local scale. Other spaceborne sensors with sub-metric ground sampling distance and/or daily revisit time would be probably suitable; however, so far, this option would need the use of commercial solutions with a consistent increase of the costs of the investigation.

- First attempt to evaluate whether Sentinel-1 data can provide quantitative estimates of fluvial morphological changes;
- Multitemporal comparison of Sentinel-1 backscattering and coherence data against UAV-SfM 3D point clouds difference;
- Sentinel-1 data found to be not suitable to track relatively small morphological changes (< 2 m in the vertical direction) and the consequent changes in the surface characteristics which are typical of river dynamics;
- SAR-based detection of fluvial changes in rivers are intrinsically affected by severe limitations due to varying soil water content and vegetation cover;
- Higher resolution and/or different spectral sensor may lead to different results but would require important acquisition costs.

Introduction

The identification and quantification of morphological changes occurring in river channels over large spatial scales and at different moments in time are essential to understand rivers behaviour, assess sediment budgets, evaluate effectiveness of river management strategies and support the production of fluvial geomorphic hazard maps (Wheaton et al., 2013, Mueller and Pitlick, 2013, Aderson and Pitlick, 2014). During a geomorphically-active fluvial event, bed-material sediments are mobilized by competent flows from an initial area (erosional site) and are transported downstream until they stop, at least temporarily (depositional sites). Beside changes in vegetation cover, the areas subject to morphological modifications associated to erosion of standing vegetation and deposition of stranded woody material show different characteristics in terms of surface roughness and curvature (Lu et al., 2004, Plank, 2014). A high-frequency, multi-temporal monitoring of surface changes in rivers would thus permit the observation of discharge-related thresholds for morphological changes, as well as to calibrate and validate numerical morphodynamic models in an unprecedented manner.

Change detection analyses through time can be used to study morphological changes caused by geomorphic processes. A straightforward approach aims at directly measuring elevation changes from sequential topographic data (at meter and sub-meter resolutions) conducted in multi-temporal remote sensing surveys. This can be done with a variety of technologies, ranging from aerial photography and photogrammetry (Lane et al., 1993, Lane et al., 2003, Rumsby et al., 2008, James and Robson, 2012); satellite photogrammetry (e.g. Pleiades, WorldView); photogrammetry based on the Structure from Motion (SfM) technology, largely applied with aerial UAV imagery (Mancini et al., 2013, Wallace et al., 2016, Marteau et al., 2017, Carrivick and Smith 2018); LiDAR (light detection and ranging or laser induced direction and ranging) technology

(Cavalli et al., 2008; Anders et al., 2013). Morphological changes can be assessed through sequential acquisition of topographic surfaces in 3D or 2.5D (Passalacqua et al. 2015). The resulting multi-temporal digital elevation data can then be compared with a range of methods based on either raster elevation data (Lane et al., 2003, Wheaton et al., 2010, 2013, Williams et al., 2015, Micheletti et al., 2015, Cucchiaro et al., 2019); or 3D point cloud (PC) comparison (James et al., 2017; Bearzot et al., 2022). The latter approach has been reported to have higher accuracy as well as an easier workflow in the case of a direct 3D PC comparison (due to the absence of surface meshing or Digital Elevation Model (DEM) generation), especially in the context of rough complex topographies (Lague et al., 2003).

The approaches listed above can be efficiently used to infer sediment budget and channel morphology (Wheaton et al., 2010, Wheaton et al., 2013, Mueller and Pitlick, 2013, Aderson and Pitlick, 2014). Despite, their availability is limited in terms of spatial extent and number of acquisitions because of high costs for each acquisition. Space-borne remote sensing could be considered as a straightforward pathway to scale up such change detection methods. Many studies have focused on the use of optical imagery from both airborne and spaceborne platforms to study morphological changes (Lane et al., 2010; Strick et al., 2018). Multitemporal optical images (from satellites, such as Landsat and Modis) have been used to derive for instance NDVI image time series and to show the dynamic changes of the probably flood-affected regions or landslides events (Fiorucci et al., 2019, Lu et al., 2004).

Synthetic aperture radar (SAR) has been widely used to monitor changes on the Earth's surface produced by natural and human-induced processes. This technology has the advantage of being mostly unaffected by weather conditions (e.g., cloud cover, strong winds) and by light conditions

(e.g., time of the day; shadows). The differential interferometry technique (DInSAR) exploits the phase difference among image pairs and can be used to measure surface displacements through time (Ferretti et al., 2001, Manzo et al., 2013). However, this technique is not applicable when large and rapid changes of the surface characteristics occur (Casu et al., 2011, Manconi et al., 2018). On the other end change detection approaches have been applied to SAR datasets to map events in several geographic and geological contexts, by exploiting both the coherence and the backscattering of the radar signal. This is the case of events like landslides (Mondini, 2011, Mondini et al., 2018), snowmelt (Nagler et al., 2016), debris flow (and/or lahar in tropical environment: Bennet et al., 2018), floods (Clement et al., 2017, Giustarini et al., 2016, Grimaldi et al., 2016, Grimaldi et al., 2020) and channel dynamics (erosion and deposition, Ullmann et al., 2016). The rationale behind is that sudden events such as earthquakes, landslides, and floods cause extensive changes in SAR signal properties (e.g., backscattering intensity and phase coherence) between images acquired before and after the event (Lu et al., 2004, Plank, 2014).

Methods exploiting changes in radar backscattering rely on the strength of the signal, which depends on dielectrical and geometrical properties of the surface (Rosen et al., 2000, Prati et al., 2010). For natural targets, this is mostly associated to changes of the land cover structure, of the surface roughness, and of the soil moisture content (Mondini 2017, Clement et al 2017). For instance, landslides alter the soil surface and remove the vegetation along path. Vegetated surfaces have different properties from bare ground (e.g., the dielectric value of the backscattering material, roughness, water content, etc.), and thus the backscattered amplitudes recorded by the pre- and post-event SAR images can change, thus helping to detect landslides (Mondini et al., 2021, Sivasankar et al., 2021). In riverine environments, change in the backscatter properties of the surface can be due to sediment movement or changes to the dielectric constant of the surface, such

as soil moisture (Olen and Bookhagen, Lu & Meyer, 2002). Alternately to radar backscattering, phase difference between two acquisitions can be exploited for change detection analysis in multi-temporal SAR data. This approach exploits coherence (or phase correlation) of image pairs selected before and after a known event (landslide, earthquake, etc.) to detect and map the spatial extents of changes occurred (Matsuoka & Yamazaki, 2004, Yun et al., 2015, Olen & Bookhagen, 2018).

In this work we explore the above outlined ideas by relying on data freely available delivered by the ESA Copernicus program of satellites. Specifically, Sentinel-1 Satellite (S-1) imagery of ESA's Copernicus Mission delivers C- Band Synthetic Aperture, at 12 days frequency (6 days in Europe between 2017 and 2021). This SAR data have been largely used for change detection, but only rarely tested in fluvial environments (Ullmann et al., 2016, Purinton and Bookhagen 2020, Olen and Bookhagen 2020). For example, Ullman et al. (2016) measured changes in amplitude and coherence to identify surface disturbances, mass movements and fluvial dynamics, in the surroundings of the Damghan Playa (North-eastern Iran), showing potentials and limitations of this approach. However, in their study, validation of radar-inferred geomorphic changes was only qualitative, and indeed the authors, highlighted the importance in future research to use in situ data regarding both the actual channel dynamics and the spatial-temporal distribution of rainfall events potentially responsible for geomorphic changes.

In this work, we investigate the performance of change detection analysis based on correlations between morphological changes measured from high resolution drone acquisitions and time series analysis of Sentinel-1 data. The analysis was performed in the Po River (Northern Italy) and aimed at testing if a change detection approach in rivers can be based either on radar intensity

and/or coherence data.

We used the standardized technique of 3D point cloud distance from UAV imagery to identify the areas affected by morphological changes in our study area. It is important to highlight that we did not aim at evaluating the accuracy in the quantification of elevation changes by satellite radar data, but only at understanding if the areas which underwent morphological changes could be detected and classified accordingly. This refers to mapping the spatial extent of morphological changes in rivers, using UAV-derived 3D point cloud differencing as ground-truthing, but – again – only in semi-quantitative terms (erosional/depositional vs stable areas). The ability to rapidly detect where channel morphological processes have occurred and their expected intensity would permit to prioritize more detailed field campaigns by, for instance, UAV technology providing a notable advance compared to the current ability to monitor river morphological changes and correspondent river sediment balance at large scale.

Material and Methods

2.1 Study Area

We selected a relatively large (0.3 km^2) sediment bar along the Po River, close to the confluence with the Tanaro River (Piedmont Region, north-western Italy, Fig. 1) as study area. Along this reach (0.3 ‰ mean slope, 0.4 km average channel width), the Po River features a wandering morphological pattern, and it is characterized by pronounced morphological dynamics. The analyzed sediment bar features a grain size in range of gravel bar (D_{50} = 35 mm).

---- Fig. 1

The site is close to a hydro-meteorological station (2.5 km downstream, named Isola Sant'Antonio) managed by the regional environmental agency of the Piedmont region (ARPA Piemonte).

152 The station which provides precipitation, river stage and discharge data at 30 min intervals. At
153 this location, the Po River drains an area of about 25,640 km² (about the 30% of the total drain-
154 age area) and features a nivo-pluvial regime (glaciated area < 1%). On average, stream flows are
155 high in spring mostly due to snowmelt, decline markedly in summer when rainfall is scarce, lo-
156 calized and mostly of convective origin, and then increase again in autumn associated to pro-
157 longed, frontal precipitations (Ravazzani et al., 2015). Such hydrological regime drivers morpho-
158 logical channel changes occurring mostly in spring and autumn when river bars – including the
159 one investigated here - are partially or completely inundated. More information on the Po River
160 can be found in Gumiero et al. (2022).

161 In this study, we analyzed morphological changes occurred from September 2017 to September
162 2018. In this period, a moderate flood event (discharge about 1,000 m^3s^{-1}) occurred on the 12
163 March 2018, which determined important in-channel changes (areas of erosional and deposi-
164 tional processes), visible from comparison of high-resolution images taken one year apart (Fig.
165 1). The chute channel has been inundated for the whole spring season 2018 and later slowly
166 dried up in the summer (the evolution of the bar is shown in detail in figure 12). Figure 2 shows
167 drone images taken in the study site respectively in September 2017, April 2018, September
168 2018 and a zoom of the chute channel created after the flood event.
169 ---- Fig. 2

170 ***2.2 Morphological changes identification by 3D point cloud differencing***

171 The morphological changes occurring in the study site were assessed by repeated high-resolution
172 elevation data. Two sequential UAV acquisitions were conducted on the river bar on the 16 Sep-
173 tember 2017 and on the 20 September 2018. A further acquisition was made on the 17 April
174 2018, when the chute channel was active. This later acquisition was used for photo interpretation

purposes only. A DJI Phantom 4 Pro drone was used for images acquisition, acquired at 80% forward overlap and 50% side overlap, at around 50 m above ground level. The drone was flown with constant forward motion leading to adjacent lines having convergent camera angles. For example, if the first line was flown from east to west, the second line was flown from west to east with 50% side overlap. RGB imagery was collected with the camera at 30° from nadir for the whole site. In addition, additional images at 80 m altitude were acquired with the camera facing outworld with an angle of 60 degrees from nadir to provide further oblique views to reduce systematic errors (Sanz-Ablanedo et al., 2020).

Prior to the flights markers were deployed on the ground of the whole study area and their coordinates were measured at cm-accuracy with a Trimble R10 differential GNSS rovers running in real-time kinematic (RTK). A total of 9 target points and 20 target points were measured respectively for the two acquisitions (2017 acquisition covered an area smaller than 2018). Approximately 60% of the Ground Control Points (GCPs) were used to georeference the orthophoto and DEMs at cm-accuracy; the remaining 40% (Check Points – CPs) was used for the validation of the generated models. This combination of convergent views with cm-accuracy ground control has been found to deliver the best possible results from drone-based SfM photogrammetry (Sanz-Ablanedo et al., 2020; James and Robson, 2014, James et al., 2017). The GCPs used were 6 for the 2017 and 14 for 2018 surveys, while the CPs were 3 (2017), 6 (2018). Agisoft Metashape software Professional Edition, version 1.6, was used to process all UAV images and to generate the 3D point cloud of each acquisition and the ortophotos useful for photo interpretation. The ground resolutions obtained are of 2 cm/pixel for 2017 and 2018 acquisitions; the coverage areas are 0.16 km^2 and 0.34 km^2 for 2017 and 2018 respectively. The accuracy of the UAV derived products was estimated by the Root Mean Square Error (RMSE) and standard deviation of errors

198 of the GCPs and the CPs. Table 1 reports these metrics for the two acquisitions.

199 ---- Table 1

200 As it can be seen, pixel resolution is comparable to the standard deviation of the CPs errors along
201 z direction, confirming that the bundle adjustment worked well. Furthermore, the ratio among
202 such error and the flight altitude accounts for 0.000542 (for 2017) and 0.00065 (for 2018) <
203 1/1000. Overall, our quality analysis indicates that our errors are of centimetric scale. The open-
204 source software CloudCompare (version v2.11 alpha) was used to compute the difference be-
205 tween the 3D point cloud extracted from Agisoft Metashape. We used the standardized proce-
206 dure included in the M3C2 plugin to measure the difference in elevation between the two acqui-
207 sitions (Lague et al., 2013, James et al., 2017). M3C2 operates directly on point clouds, com-
208 putes the local distance between two point clouds along the normal surface direction, which
209 tracks 3D variations in surface orientation. In addition, the plug-in generates a significant change
210 map: for each distance measurement, it commutes a confidence interval depending on point
211 clouds registration error (Lague et al., 2013); this map indicates whether the distance correspond
212 to a real change or not, with a confidence level of 95%. We compute the distances using as refer-
213 ence the 2018 dense cloud. M3C2 algorithm can be used in 2D by imposing a vertical normal
214 calculation which is equal to the standardized DoD method without the need for gridding (DEM
215 generation).

216 For determining the vertical uncertainties (Brasington et al., 2003; Lane et al., 2003, Wheaton et
217 al. 2010) we estimated the root mean square error (RMSE) and the standard deviation (STDEV)
218 of the surveyed check points (Milan et al., 2007) along the z direction (Tabella 5.1). For appro-
219 priate error propagation into the topographic analysis made, we used the CPs STDEVz of the dif-
220 ferent surveys to enable the significant changes to be estimated with the formula (1):

$$LoD_{95\%} = \pm 1.96 \cdot \sqrt{{\sigma_{z1}}^2 + {\sigma_{z2}}^2} \qquad (1)$$

where: LoD is the Level of Detection to represent a 95% confidence level, for which, under t distribution, t=1.96; σ_{z1} and σ_{z2} are the STDEV along the z direction for 2017 and 2018 acquisition respectively. Surface changes are considered statistically significant when exceeding the $LOD_{95\%}$ value (Lane et al., 2003, Lague et al., 2013, James et al., 2017). We obtained a $LOD_{95\%}$ of ± 0.08 m, thus all morphological changes greater than ± 0.1 m are statistically significant and can be distinguished from the intrinsic "noise" relative to the surveying methods. For our analysis, we decided to use a threshold which was higher than this error, i.e., equal to ± 0.5 m, to select only areas subject to marked vertical changes. This choice was driven by the limits of Sentinel-1 in terms of spatial resolution, as well as by the intention to avoid vertical changes in the order of the surface roughness, i.e., to consider bed variations > 5-10 times larger than the median surface sediment size (D_{50} of about 40 mm). The areas exceeding such thresholds were then manually delineated and excluded by using the 'filter by value' option in Cloud Compare, exported and later used in QGIS as masks on Sentinel-1 radar raster.

As said in the introduction, the aim is not to compare elevation changes magnitude measured by UAV against the radar data. Our intent is to investigate whether radar-derived information can be associated to river areas which underwent erosion, deposition or remained stable, based on different surface characteristics (changes in structure, geometry, roughness, vegetation cover) before and after a flood event.

2.3 Sentinel-1 data processing and extraction

Sentinel-1 data were downloaded from the Copernicus Open Access Data Hub (https://scihub.copernicus.eu/dhus/#/home) in L1 Single Look Complex (SLC) mode and pre-processed within the

Sentinel Applications Platform (SNAP) software, version 8.0 (step.esa.int/main/toolboxes/snap/). A single SLC product contains information about the radar return wave stored as complex numbers, with two parts: the amplitude or intensity of the return (dependent on surface geometry, roughness, and dielectric characteristics) and the phase of the return in radians (from 0 to 2π), depending on the distance the signal has travelled. The SAR images used in this study belong to path number 15, ascending orbit and were acquired with a temporal separation of 12 days by Sentinel-1B, for a total of 58 dates, selected from January 2017 to December 2018. The processing steps, applied in SNAP in a batch process, are summarized in figure 3. The pre-processing differs for intensity and coherence data generation. The data were projected to a common grid (World Geodetic System (WGS) 1984, Universal Transverse Mercator (UTM) Zone 32 North). As regards backscattering, primary co-registration (S1 Back Geocoding) of the 58 images was applied by selecting as primary image a date in the middle of the time series (12 January 2018). Speckle Filter using a moving window of 5 by 5 pixels was then applied to mitigate noise, and finally a conversion from backscattering values to gamma nought (γ_0) in decibels (dB).

Formulation of gamma nought is reported on the Sentinels Copernicus documents for Radiometric calibration as (2):

$$\gamma_0 = \frac{DN^2}{A_\gamma^2} \qquad (2)$$

Where $A\gamma$ is reported in the Look Up Tables (LUT) and used to transform the radar reflectivity into gamma γ_0 where the area normalization is aligned with a plane perpendicular to slant range; DN is the pixel Digital Number being, in the case of SLC: the pixel amplitude defined as

$\sqrt{I^2 + Q^2}$ where I and Q are the real and imaginary values from the measurement file. The outputs of the processing are two raster stacks, at 13.95 m/pixel, respectively with VV and VH polarizations, composed of 53 bands (i.e., dates analysed in the time series). The terrain corrected gamma nought intensities of the VV and VH channel were used in the analysis.

In parallel all SAR images co-registered were debursted and multilooked (2 azimuth and 7 range), and subsequently used to calculate interferometric coherence within a 7×7 pixels window. In this study, we calculated coherence pairwise between temporally adjacent images: {(date$_1$ date$_2$]), (date$_2$ date$_3$), … ,(date$_{N-1}$ date$_N$)}. Output of the pre-processing are two rasters at 13.95 m/pixel resolution reporting 52 bands (coherence pairwise between temporally adjacent images) for the coherence data raster.

The interferometric coherence is calculated between two SAR images collected from the same location at different acquisition times, estimated by their spatial correlation, defined as (3):

$$Coherence = \frac{E(s_1 s_2^*)}{\sqrt{E(s_1\, s_1^*)E(s_2 s_2^*)}} \qquad (3)$$

where s_1, s_2 are the complex pixel values at times $t = 1$ and $t = 2$; $s*$ is the complex conjugate of s, and E is the ensemble average (Bürgmann et al, 2000).

From the full radar raster of the temporal series examined (at 13.95 m/pixels spatial resolution), subsets of the zones interested by different morphological changes were conducted in Python (with fiona and rasterio libraries). These sets were defined as follows: ‘Erosion’, ‘Deposition’, ‘Stable’, ‘Control’ depending on the main process identified. ‘Control’ sets, were selected in mixed land cover areas, outside of the sediment bar, and used as reference, for comparison with the geomorphic active zones in the river bar. This kind of comparison is recommended when

working with intensities and coherence radar data, to be sure that results obtained are effectively linked to the process we want to discriminate and no to other possible noises linked to the radar acquisition. The vector created were used as a mask, to extract pixels belonging to each zone. Figure 3 reports the workflow followed for Sentinel-1 backscattering data extraction in each zone.

--- Fig.3

2.4 Optical imageries and hydro-meteorological data

As already mentioned, in the study area we could rely on hydro-meteorological data registered at the Isola Sant'Antonio gauging station. A moving average on daily rainfall data was used to compute the cumulated rainfall in the antecedent days, a factor controlling soil moisture content of the analyze river bar, in addition to river stage fluctuations. The daily water level was calculated from the water level data registered at 30 min intervals from the station, in the 58 dates of the Sentinel-1 images downloaded. The water level helped track river flow variability and the correspondent inundation of the bar during the monitored period.

High-resolution satellite imagery at 3 m resolution (obtained from planet.com) were used to document and interpret morphological changes from the reach to the bar scale during the analyzed period (as shown in Fig. 11). Orthophotos at 10 cm/pixel, generated during the photogrammetric analysis of the drone imagery, were also useful as they allowed us to analyze changes at the subunit scale with a higher accuracy.

Results

3.1 Geomorphic changes detected by UAV-based distance map

Figure 4 reports the distance map (between the point clouds of September 2017 and September 2018), obtained via the M3C2 plugin, together with the significant change map with a level of

confidence of 95%.

--- Fig. 4

Morphological changes evidenced by the cloud-to-cloud distance are mostly located in the portion of the bar where the chute channel was formed in March 2018 (during the moderate flood event described in section 2.1). The areas affected by major changes (> ± 0.5 m) are represented by: i) the above mentioned, newly formed chute channel (see figure 2 for a zoom of the eroded channel), visible in red color; ii) the small portion of the bar, located on the right side of the chute channel, where deposition occurred. Except for these areas, the sediment bar remained largely unchanged or underwent subtle variations (values of significant change of around < ± 0.1 m). It must be noted that areas located at the border of the acquisitions were not considered due to the lateral deformation as well as for the presence of tall vegetation.

Despite in May and June 2018 the entire bar was repeatedly inundated (flow discharges around 1,200 m^3s^{-1}, as visible from planet.com images, see later in Fig. 11), changes over most of the bar were not linked to bed-material transport but rather to the removal of low vegetation and fine material deposition. Vegetation was present on the bar as low (<0.5 m) and sparse shrubs. By comparing the orthophotos taken one year apart (see Figures 1 and 12), a more diffuse presence of small vegetation is visible in September 2018, whose growth was most likely spurred by the inundation of the bar in the previous spring season. The chute channel formed in spring 2018 (see Figure 2b), reactivated a former channel, which was covered with algae and short vegetation at the time of the first acquisition (see Figure 2a). Later, in September 2018, ponding was observed in the deeper part of the chute channel, which became hydrologically disconnected – at least at the surface - from main low-flow channel. In the M3C2 distance calculation, the presence of water may lead to erroneous results in terms of elevation difference (Westaway et al., 2000).

This is the reason why in the analysis we did not consider results located in wet areas in 2018.

As already mentioned in the Methods section, to delineate polygons relative to the areas of the river bar subject to erosion, to deposition and to negligible changes (hereafter called "stable") we preferred to consider a threshold of ± 0.5 m for separating stable vs change (erosion or deposition) despite the 3D model error being lower (see section 2.2). This threshold was chosen to meet the requirements of considering in the analysis only the largest morphological changes measured and guarantee enough Sentinel-1 pixels included in each zone. In this way we also accounted for possible additional errors due to the presence of vegetation growing on the bar, and to bed variations in the order of the median surface sediment size (D_{50} about 40 mm). The masks identified as erosion and deposition, using the 'filter by value' option with a threshold of ± 0.5 m, fall into the zones where significant changes are measured (see significant changes $LOD_{95\%}$ map of figure 4d). Following this procedure, the area of erosion considered in our analysis is of 8'417 m²; depositional area is smaller (2'051 m²); the stable area selected for comparison accounts for 10'706 m².

3.2 Investigating the relation between geomorphic changes and radar intensity

The selected areas were used as masks on the Sentinel-1 processed images to extract intensity values of each area. A total of 43 Sentinel-1 pixels were included in the "Erosion" area; 10 pixels in the "Deposition"; and 55 pixels in the "Stable" one. Figure 5 reports the boxplot of the intensity values (expressed as mean of VV and VH polarization) of the three zones pre and post the flood event, respectively on the 2 of September 2017 and on the 20 of September 2018 (close to the ground truth dataset acquisitions).

--- Fig 5

The t-test revealed that in the two dates, there is a statistically significant difference between the pre and post images, a year later, in deposition and erosional areas (p-value < 0.001) while not for the stable area. However, the difference in the intensity values of the three areas is within the expected errors of the analysis performed. Therefore, it is not possible to discriminate changes associated to other factors than noise. In fact, the variability of the intensity data during the monitored time interval amounts to about 10 dB (from -8 to -18 dB): the difference is therefore in the range of ± 5 dB of the central mean value. Despite in 2017-2018 there are some differences, they are lower or within this range of ± 5 dB. This means that it seems not possible to discriminate between areas where morphological changes occurred (erosion and/or deposition) from areas that remained stable one year apart. Figure 6 shows the spatial variability found in the three areas in the change detection approach, by comparing in a RGB false colours pre- and post- event images (same dates used in figure 5).

---- Fig 6.

This analysis allows us to highlight the difference in terms of backscattering between the 2 dates analyzed: in red colour are represented those pixels where the backscattering has increased in 2018; in light blue colour where the intensity has decreased (for instance for the presence or increase in water content) in 2018. Comparing this image with the high-resolution orthophotos taken from drone, lateral/bank erosion is observed to be detected by this analysis, as the erosion of the upper part of the bar, close to the main channel, as well as the exposure of a greater portion of the sediment bar on the other side of the channel are correctly picked. However, looking at the spatial distribution of the backscattering in the three areas, we cannot distinguish if changes occurred or not.

To make sure these variations were not date-specific, a time series analysis was carried out to investigate the seasonal variability in the backscattering response, thereby to understand possible factors (site- specific and time dependent) that may influence the backscattering (soil moisture, grain size distribution, vegetation). Figure 7 shows results of the time series analysis, reporting the backscattering values in all season and dates selected.

---- Fig 7

Dark Gray stars indicate the dates of figure 5-6; Gray dashed lines delimit the period when the bar was partially or entirely inundated (see figure 11). Over the time monitored, the three areas present similar fluctuations in the Sentinel-1 radar backscattering registered, with some differences at specific dates. In 2017 depositional areas present overall lower intensity values. A specific trend is visible for erosional/depositional areas in comparison to the stable area, during the period of high-water discharge registered in spring season 2018. Afterwards, throughout summer and late autumn 2018 there are not specific differences among the areas. The backscattering signal registered by Sentinel-1 seems therefore able to detect some land cover changes but not to clearly distinguish the morphological changes detected by the high-resolution 3D point cloud differencing. Results shown in Figure 6 report the mean value of all pixels belonging to each zone. Pixels of each zone may include portion of small vegetation cover and/or water content and the mean value could be influenced by these factors. An expert-based selection of one pixel per area was therefore made to reduce the influence of disturbing factors as much as possible. In the stable, erosion and deposition area, pixels of bare soil were selected with the help of the high-resolution drone imagery. Also in this case the trend was similar, and we do not show such results for sake of conciseness.

398 In addition, to better interpret the above results and their reliability, and to exclude disturbing ef-
399 fects of the recorded signal, the analysis of the trend of backscattering values in areas other than
400 the area of interest could be informative. Two areas were selected as reference (named 'Control'
401 areas) to see the response recorded by the sensor in the surroundings of the sediment bar (Fig. 8).

402 ----- Fig 8.

403 In the 'Control' areas, composed of mixed land cover (buildings, trees, fields, roads), backscat-
404 tering values follow a pattern close to what detected in the stable area (see Figures 7). This
405 shows that Sentinel-1 intensity values are influenced by factors common to all the 5 areas con-
406 sidered in our analyses (3 identified in the study site and 2 selected as reference).

407 ***3.3 Investigating the relation between geomorphic changes and radar coherence***

408 The selected areas were used as masks on the Sentinel-1 processed images to extract coherence
409 values of each area, calculated within a moving window of 7x7 pixels. Surface changes follow-
410 ing an event is generally performed via a comparison of pre-event and syn-event (i.e., compari-
411 son of one SAR image before and one image after the event) coherence images. A complete loss
412 in the coherence value (value close to 0) can be caused either by large changes in the phase of
413 the radar signal (e.g., surface-elevation changes in the direction of the satellite line-of-sight) or
414 by changes in the signal's amplitude (e.g., change in the backscatter properties of the surface due
415 to sediment movement or vegetation growth and changes to the dielectric constant, such as soil
416 moisture). Relying on a single pre-event coherence estimate (i.e., from a single SAR pair) ne-
417 glects the natural variability in the SAR coherence signal through time for different land covers
418 and climatic regions so that a coherence time series analysis is useful to consider these aspects.
419 Figure 9 shows results of the time series analysis, reporting the coherence values in all image

pairs selected from January 2017 to December 2018.

---- Fig.9

Over the time monitored, the three areas present similar fluctuations in the Sentinel-1 coherence values measured, following all very close patterns. No specific trends and coherence loss linked to surface changes are clearly distinguishable through time for erosional/depositional processes in comparison to the stable area throughout the two years examined. The same analysis was performed by selecting, expert-based, one pixel per area (same pixels used for the intensity analysis), to reduce the influence of disturbing factors as much as possible. Results are like what obtained considering all pixels included in each zone. Moreover, the plot of coherence value registered in the 'Control' areas was conducted for comparison and reported in Figure 10.

---- Fig 10

Coherence time series in the two areas selected outside the site follow similar pattern to those measured for erosion/deposition and stable areas. The two control areas show different pattern in the coherence values between 25 March 2018 to 9 September 2018.

4. Discussion

The analysis performed in the Po River aimed at testing if a change detection approach could be developed exploiting either radar intensity and/or coherence data The analyses of Sentinel 1 time series data showed (see sections 3.2 and 3.3) that the Sentinel-1 intensity and coherence data were poorly sensitive to the geomorphic activity of the channel. This means that, despite Sentinel 1 derived data are somehow sensitive to the presence of changes in the surface characteristics, the capability to discriminate a change is not yet satisfactory from a fluvial geomorphological

perspective.

The results reported in this work use Sentinel-1 backscattering and coherence data expressed as the mean of the VV and VH polarizations, because we did not see any reason to prefer one polarization over another, as results were very similar. We also tested the analysis by using the sum of the two polarizations VV and VH to emphasize possible differences among the areas. In all attempts, we find no significant differences among the intensity trends for the three areas identified – erosion, deposition, stable. We also attempted the use of the Log Ratio analysis of intensity data proposed by Mondini et al. (2017) to further elaborate the data but trends were almost the same as the other analyses made. In addition, two areas were selected as reference (named 'Control' areas) to see the response recorded by the sensor in the surroundings of the sediment bar. The 'Control' areas backscattering, and coherence values (Fig 8-10) follow a pattern very close to that of all other zones (see Figures 7-9) despite they are composed of mixed land cover (buildings, trees, fields, roads). This confirms that Sentinel-1 data are influenced by other factors, common to all the 5 areas considered in our analyses and that variations are not linked to the morphological changes occurred. Other tests have been conducted also using different pre-processing options and parameters in SNAP (e.g., No multitemporal speckle filtering) on the raw radar data, but results were very similar.

4.1 Possible explanation for radar data variations

4.1.1 Possible influence of hydro-meteorological factors

To support the understanding of the trends found in the intensity and coherence values, the hydrometeorological data of the upstream gauging station were used, for all dates for which

462 Sentinel-1 data were available (Figure 11), to assess the contribution of rainfall events in the
463 backscattering response. Rainfall events are expressed as the average of all precipitation events
464 occurred in the previous 12 days (or more in case some Sentinel-1 date were missing), thus the
465 value consider the total amount of rain fell till the specific date.
466 ---- Fig. 11
467 Overall, from literature, we expect a decrease in the backscattering values when the water con-
468 tent in the top sediment layer increases. It is thus usually expected a decrease in the backscatter-
469 ing values registered by the sensor after a high rainfall value, because of a modification in the di-
470 electric characteristics of the soil (Rosen et al., 2000, Clement et al., 2017). Looking at the rain-
471 fall data and at the correspondent intensity values, no rainfall event (even the most significant
472 such as those occurred in 01.11.2017) seems to have determined a decrease in the backscattering
473 registered by Sentinel-1 (Figure 7). Similar consideration are valid for coherence time series
474 analysis where a loss in coherence may be linked to several reasons: it can be determined either
475 by large changes in the phase of the radar signal (e.g., surface-elevation changes in the direction
476 of the satellite line-of-sight) or by changes in the signal's amplitude (e.g., change in the backscat-
477 ter properties of the surface due to sediment movement or vegetation growth and changes to the
478 dielectric constant, such as soil moisture). A possible reason for the lack of a consistent correla-
479 tion between backscattering and coherence and precipitation could be the intrinsic nature of the
480 fluvial deposits. In fact, bar sediments can become wet not only because of local rainfall events
481 but also by water flows that inundate the bar due to increased runoff generated in the upstream
482 basin, thus the spectral response may not change significantly after a rainfall event. Moreover,
483 large uncertainties limit the soil moisture retrieval from SAR backscattering (Dubois et al., 1995,
484 Doubková et al., 2012, Rawat et al., 2017). In general, the quantification of the respective

485 contributions of all factors that influence the backscattering coefficient and coherence trends is a
486 challenging task and more than one combination of sediment/soil characteristics leads to similar
487 electromagnetic responses at the sensor, thus making ground target characteristic complex to de-
488 termine.

489 Different considerations can be made when looking at the correlation with radar derived data and
490 the water level data. The opening of the secondary channel occurred on the 12 of March 2018,
491 when water stage shows a first peak at around 2 m (on 13.03.2018). The highest water stage
492 (about 3 m) was registered on 30.04.2018. At this water level, the areas identified as Erosion and
493 Deposition were inundated until mid-June 2018 (water stage around 2.3 m in average), as con-
494 firmed from the high-resolution Planet.com satellite images (Fig. 12). Under such conditions,
495 based on the available knowledge, we expect a decrease in the radar intensity values, therefore
496 the decrease in radar intensity evident from figure 7 is consistent with this explanation. Indeed,
497 when the radar signal encounters a water body, which acts almost like a specular reflector of the
498 radar pulses, the resulting signal returned to the satellite is minimal (Clement et al., 2017;
499 Schlaffer et al., 2017, Giustarini et al., 2016). However, the radar intensity values in the ana-
500 lysed area of the Po River were not affected by the flood event occurred in autumn 2018. From
501 literature we know that the presence of local turbulences, small waves, woody debris transported
502 in the secondary channel, can roughen the water surface thus increasing the portion of the signal
503 returned to the sensor. These kind of effects, together with heavy rainfall and wind, are reported
504 in literature among the main limits encountered to detect floods and water bodies from radar data
505 (Alsdorf et al., 2007, Clement 2017, Giustarini et al., 2015, Rossi ed at., 2023). These reasons
506 could explain why there is not always a consistent trend mirroring the variations of water stage.

507 Similar considerations can be made for the interpretation of coherence data loss. In the analysis

made, following a change detection approach (Walter et al., 2014, Olen and Bookhagen 2020), we expect a low coherence value (close to 0) for all image pairs that present different conditions in the two dates considered (different surface characteristics, water content, land cover). Conversely, value close to 1 is expected when the three areas were characterized by similar conditions in the dates considered (usually happening in urban areas or desertic regions). However, only few coherence losses are clearly related to rainfall events and to the inundation of the bar. Specifically, when the first moderate flood event (discharge about 1,000 m^3s^{-1} occurred on 12 March 2018 determining the creation of the chute channel on the bar analyzed in this study (fig. 1 and fig. 2), the areas delineated as 'Erosion' and 'Deposition' were affected by the water flow while the 'Stable' area was not. The pre- and post- event image pair to be considered (1st of March – 13th of March 2018) show a coherence loss from around 0.7 to 0.3 for the morphologically active areas, while the stable area remained at a constant coherence value. Later, in April, the water level increased causing the inundation of the whole bar for a couple of days. For this event the image pair to be considered is the 6-30 of April 2018, and in this case a coherence loss from around 0.8 to 0.2 was measured for the three areas. Beyond the above-mentioned examples, overall, the fluctuations observed in coherence data are not clearly linked to the morphological activity of the channel.

4.1.2 Comparison with high-resolution RGB images

We used orthophotos at high-resolution (10 cm/pixel) drone (DJI Phantom 4) imagery and RGB high-resolution (3 m/pixel) satellite (planet.com) imagery to support results interpretation by watching the bar inundation dynamics and pattern associated to varying water stages. Figure 12 reports planet.com imagery in some representative dates of the two years investigated, for

comparison.

---- Fig. 12

As confirmed by photo interpretation of RGB Planet, the secondary channel remained active from April 2018 till June 2018 (in the 30.04.2018 the water level reached a pick of about 3 m see figure 11). In September 2018, when the second drone flight acquisition was conducted, dry conditions were present on the whole sediment bar. In the 8.11.2018 the water level showed a pick higher than 3 m (see Figure 11), but we do not know which portion of the bar was inundated because of highly clouds coverage in November. It is likely that again the two areas 'Deposition' and 'Erosion' had been inundated at that time, but it is not possible to have a confirmation from photo interpretation. If that were the case, as mentioned in the previous paragraph, there are several factors that may explain why this event was not detected by the radar derived data used. Specifically, the effectiveness of Sentinel-1 to map flood events occurring in different European river basin can roughly achieve the 30% of the total events (Tarpanelli et al., 2022). This percentage may be even less if we address the challenges mentioned above and require sufficient quality (Tarpanelli et al., 2022, Schumann, 2021).

Figure 13 shows a zoom of the orthophotos at 10 cm/pixel on the three zones. Looking into the details of the evolution through time of the three areas, it is evident that they are in different conditions and have changed surface characteristics.

---- Fig 13

By comparing the orthophotos taken one year apart (Figures 1, 13), a more diffuse presence of small vegetation and algae is visible in September 2017 in the depositional area, whose growth was most likely spurred by the inundation of the bar in this portion in the previous spring season. In this date (14-26.09.2017) and starting from January 2017, the backscattering values of the

553 depositional area are lower (see figure 7), mirroring the possible presence of higher water con-
554 tent in comparison to the other areas.

555 However, after the flood event that took place in spring 2018 causing the morphological changes,
556 the backscattering values in the corresponding time (09-21.09.2018, Fig. 7), in each zone charac-
557 terized by different surface changes, are rather similar. For instance, in September 2018, pond-
558 ing was observed in the deeper part of the chute channel ('Erosion' area), which became hydro-
559 logically disconnected – at least at the surface - from main low-flow channel. However, intensity
560 values of all areas have similar values, including for the 'Control' area, characterized by a com-
561 pletely different land cover. Despite the different surface cover, the zones selected respond in the
562 same manner.

563 ***4.2 Open challenges and future developments***

564 Overall, the analysis of Sentinel-1 backscattering and coherence data revealed some correlation
565 with the inundation dynamics of the sediment bar investigated here. However, the variations
566 found in the time series analysis of the Sentinel-1 data were poorly linked to observed morpho-
567 logical changes and to hydrological data measured. Despite the morphological changes measured
568 from high-resolution data are significant from a statistical and geomorphological point of view
569 and can easily be measured with high-resolution data, they revealed to be not enough to be re-
570 trieved from Sentinel-1. In general, and especially for SAR data analysis, the larger is the area
571 investigated and the higher is the event magnitude, the more results are good. The backscattering
572 can assume a wide range of values (dB scale); significant variation in the backscattering values is
573 needed to detect changes. One of the main open challenges in this context is to have information
574 about the threshold that discriminate the magnitude of events detectable from satellite (Ullman

2016). In this study we demonstrated that river morphological changes in the range of ± 0.5 - 2 m occurred in a diagonal bar of a wandering river reach, for an extent less than 0.01 km^2 are not detected from Sentinel-1 data, in a change detection approach. Results obtained provide useful hints on the effectiveness of the use of Sentinel-1 to infer information about rivers morphodynamic processes, that may occur on medium-large river (e.g., active channel width ≥ 50 m) after a flood that caused significant morphological adjustments. In this context, we argue that the combination of the target size and the spatial resolution of the sensor is not suitable for this purpose. Despite the spatial and temporal resolutions of Sentinels data are greatly improved in comparison to the past satellite missions, they are not sufficient for a reliable mapping of river morphological changes, at least in rivers like the study case. Moreover, the C-band radar presents potential challenges due to its high sensitivity to surficial changes and vegetation cover, which can provide a noise signal particularly in regions with high/seasonal vegetation coverage. In comparison, the shorter wavelength X-band radar systems (e.g., TerraSAR-X or COSMO-SkyMed) that have higher spatial resolution and/or the longer-wavelength L-band radar systems (e.g., ALOS satellites) which are more stable and partially penetrate through variable surface features such as vegetation cover (but are less sensitive to surficial changes) could be used (Olen and Bookhagen 2018). However, we remind that access to SAR data from current X- and L-band systems is limited by availability and expense, restricting the applicability of SAR applications not easily accessible for a continuous monitoring.

These outcomes also highlight that, in a prospective of large-scale modelling and mapping exploiting the huge amount of spatial collected data, a rigorous validation of satellite products is essential and always strongly recommended (Schumann, 2019, Tarpanelli et al 2022). Future research should further investigate the correlation among river morphological changes and radar

598 data, by increasing the spatial resolution of the sensor (e.g., using other satellite data such as
599 Cosmo-Skymed, TerraSAR-X, ICEYE, Cappella) or by increasing the amplitude/magnitude of
600 the target (morphological changes bigger than those examined in this study). The complexity of a
601 fluvial dynamic environments with the interaction between vegetation/water/sediments through-
602 out the season is challenging. Future tests are worth to be conducted also in other environments
603 characterized by different climate condition (arid, semi-arid, semi-humid, tropical) and natural
604 processes (rivers, periglacial areas, debris flow, lahar events) where morphological changes can
605 occur at large spatial scale and involve a great magnitude of sediments and where the availability
606 of ground-truth information (monitoring data, field surveys) is present.

607 **Conclusions**

608 This work showed some of the important limitations in the use of Sentinel-1 data for change de-
609 tection monitoring in a fluvial environment. Despite the great advantage of radar data, available
610 for free, with no limitations for weather conditions, these data are not suitable to derive morpho-
611 logical changes in the range of ± 0.5 - 2 m magnitudes in a river bar. This study is the first at-
612 tempt that compare the Sentinel-1 signal to higher quality reference data (e.g., data on the spa-
613 tial-temporal distribution of the rainfall events and in situ data on the activity/inactivity of the
614 channels) in a highly dynamic fluvial environment. In such context, considering the magnitude
615 of the morphological changes examined and the resolution of Sentinel-1, it was not possible to
616 discriminate the contribution of all aspects that may influence the spectral response of the signal
617 (roughness, water content and vegetation growth). Other tests using other high-resolution satel-
618 lite and morphological changes of different magnitude, in different natural environment, may
619 lead to other conclusions. Mapping morphological changes through time at the river network
620 scale remains still an open challenge for the scientific community, but possible improvements

may come soon from higher resolution sensor and different spectral sensors.

References

Alsdorf, D.E., Rodríguez, E., Lettenmaier, D.P., 2007. Measuring surface water from space. Reviews of Geophysics 45. https://doi.org/10.1029/2006RG000197

Alsdorf, Douglas E., Ernesto Rodríguez, and Dennis P. Lettenmaier. 2007. Measuring Surface Water from Space. Reviews of Geophysics 45 (2). doi:10.1029/2006RG000197.

Anders, N. S., A. C. Seijmonsbergen, and W. Bouten. 2013. Geomorphological Change Detection Using Object-Based Feature Extraction From Multi-Temporal LiDAR Data. IEEE Geoscience and Remote Sensing Letters 10 (6): 1587–91. doi:10.1109/LGRS.2013.2262317.

Anderson, Scott, and John Pitlick. 2014. Using Repeat Lidar to Estimate Sediment Transport in a Steep Stream. Journal of Geophysical Research: Earth Surface 119 (3): 621–43. doi:10.1002/2013JF002933.

Bearzot F., Garzonio R., Di Mauro B., Colombo R., Cremonese E., Crosta G.B., Delaloye R., Hauck C., Morra Di Cella U., Pogliotti P., Frattini P., Rossini M. 2022. Kinematics of an Alpine rock glacier from multi-temporal UAV surveys and GNSS data. Geomorphology 402 (2022) 108116.

Brasington, James, Joe Langham, and Barbara Rumsby. 2003. Methodological Sensitivity of Morphometric Estimates of Coarse Fluvial Sediment Transport. Geomorphology 53 (3): 299–316. doi:10.1016/S0169-555X(02)00320-3.

Burrows, Katy, Richard J. Walters, David Milledge, Karsten Spaans, and Alexander L. Densmore. 2019. A New Method for Large-Scale Landslide Classification from Satellite Radar. Remote Sensing 11 (3): 237. doi:10.3390/rs11030237.

Carrivick, Jonathan L., and Mark W. Smith. 2019. Fluvial and Aquatic Applications of Structure from Motion Photogrammetry and Unmanned Aerial Vehicle/Drone Technology. WIREs Water 6 (1): e1328. doi:10.1002/wat2.1328.

Casu, F., A. Manconi, A. Pepe, and R. Lanari. 2011. Deformation Time-Series Generation in Areas Characterized by Large Displacement Dynamics: The SAR Amplitude Pixel-Offset SBAS Technique. IEEE Transactions on Geoscience and Remote Sensing 49 (7): 2752–63. doi:10.1109/TGRS.2010.2104325.

Cavalli, Marco, Paolo Tarolli, Lorenzo Marchi, and Giancarlo Dalla Fontana. 2008. The Effectiveness of Airborne LiDAR Data in the Recognition of Channel-Bed Morphology. CATENA 73 (3): 249–60. doi:10.1016/j.catena.2007.11.001.

Clement, M.a., C.g. Kilsby, and P. Moore. 2018. Multi-Temporal Synthetic Aperture Radar Flood Mapping Using Change Detection. Journal of Flood Risk Management 11 (2): 152–68. doi:10.1111/jfr3.12303.

Doubková, Marcela, Albert I. J. M. Van Dijk, Daniel Sabel, Wolfgang Wagner, and Günter Blöschl. 2012. Evaluation of the Predicted Error of the Soil Moisture Retrieval from C-Band SAR by Comparison against Modelled Soil Moisture Estimates over Australia. Remote Sensing of Environment, The Sentinel Missions - New Opportunities for Science, 120 (May): 188–96. doi:10.1016/j.rse.2011.09.031.

Dubois, P.C., J. van Zyl, and T. Engman. 1995. Measuring Soil Moisture with Imaging Radars. IEEE Transactions on Geoscience and Remote Sensing 33 (4): 915–26. doi:10.1109/36.406677.

Fiorucci, Federica, Francesca Ardizzone, Alessandro Cesare Mondini, Alessia Viero, and Fausto Guzzetti. 2019. Visual Interpretation of Stereoscopic NDVI Satellite Images to Map Rainfall-Induced Landslides. Landslides 16 (1): 165–74. doi:10.1007/s10346-018-1069-y.

Giustarini, L., H. Vernieuwe, J. Verwaeren, M. Chini, R. Hostache, P. Matgen, N. E. C. Verhoest, and B. De Baets. 2015. Accounting for Image Uncertainty in SAR-Based Flood Mapping. International Journal of Applied Earth Observation and Geoinformation 34 (February): 70–77. doi:10.1016/j.jag.2014.06.017.

Giustarini, L., Hostache R., Kavetski D., Chini M., Corato G., Schlaffer S., and Matgen P. 2016. Probabilistic Flood Mapping Using Synthetic Aperture Radar Data. IEEE Transactions on Geoscience and Remote Sensing 54 (12): 6958–69. doi:10.1109/TGRS.2016.2592951.

Grimaldi S., Xu J., Li Y., Pauwels V.R.N., Walker J.P., 2020. Flood mapping under vegetation using single SAR acquisitions. Remote Sensing of Environment.

Gumiero, B., B. Maiolini, F. Comiti, and F. Moroni. 2022. Chapter 12 - The Italian Rivers. In Rivers of Europe (Second Edition), edited by Klement Tockner, Christiane Zarfl, and Christopher T. Robinson, 655–83. Elsevier. doi:10.1016/B978-0-08-102612-0.00012-2.

James, M. R., and S. Robson. 2012. Straightforward Reconstruction of 3D Surfaces and Topography with a Camera: Accuracy and Geoscience Application. Journal of Geophysical Research: Earth Surface 117 (F3). doi:10.1029/2011JF002289.

James M.R., Robson S. and Mark W. Smith. 2017. 3-D uncertainty-based topographic change detection with structure-from-motion photogrammetry: precision maps for ground control and directly georeferenced surveys. Earth Surface Processes and Landforms. 42, 1769–1788. DOI: 10.1002/esp.4125

Lague D, Brodu N, Leroux J. 2013. Accurate 3D comparison of complex topography with terrestrial laser scanner: application to the Rangitikei canyon (N-Z). ISPRS Journal of Photogrammetry and Remote Sensing 82: 10–26. DOI:10.1016/j.isprsjprs.2013.04.009.

Lane, S.N., K.S. Richards, and J.H. Chandler. 1993. Developments in Photogrammetry; the Geomorphological Potential. Progress in Physical Geography: Earth and Environment 17 (3): 306–28. doi:10.1177/030913339301700302.

Lane, S. N., Westaway R. M., and Hicks D. M. 2003. Estimation of erosion and deposition volumes in a large, gravel-bed, braided river using synoptic remote sensing. Earth Surface Processes and Landforms 28 (3): 249–71. doi:10.1002/esp.483.

Lane S. N., Widdison P. E., Thomas R. E., Ashworth P. J., Best J. L., Lunt I. A., Sambrook Smith G. H., Simpson C. J. 2010. Quantification of braided river channel change using archival digital image analysis. Earth Surface Processes and Landforms. https://doi.org/10.1002/esp.2015

Lu, D., P. Mausel, E. Brondízio, and E. Moran. 2004. Change Detection Techniques. International Journal of Remote Sensing 25 (12): 2365–2401. doi:10.1080/0143116031000139863.

Mancini, Francesco, Marco Dubbini, Mario Gattelli, Francesco Stecchi, Stefano Fabbri, and Giovanni Gabbianelli. 2013. Using Unmanned Aerial Vehicles (UAV) for High-Resolution Reconstruction of Topography: The Structure from Motion Approach on Coastal Environments. Remote Sensing 5 (12): 6880–98. doi:10.3390/rs5126880.

Manconi, A., F. Casu, F. Ardizzone, M. Bonano, M. Cardinali, C. De Luca, E. Gueguen, et al. 2014. Brief Communication: Rapid Mapping of Landslide Events: The 3 December 2013 Montescaglioso Landslide, Italy. Natural Hazards and Earth System Sciences 14 (7): 1835–41. doi:10.5194/nhess-14-1835-2014.

712 Manzo M., Berardino P., Bonano M., Casu F., Manunta M., Pepe A., Pepe S., Sansosti E., Solaro
713 G., Tizzani P., Zeni G., Guglielmino F., Puglisi G., De Martino P., Obrizzo F., Tammaro
714 U., Lanari R. 2013. Analysis of the SBAS-DInSAR displacement time-series accuracies
715 retrieved in volcanic areas through the first- and second-generation sensor SAR data.
716 IEEE International Geoscience and Remote Sensing Symposium - IGARSS, 2013, pp.
717 141-144, doi: 10.1109/IGARSS.2013.6721112.
718 Marteau, Baptiste, Damià Vericat, Chris Gibbins, Ramon J. Batalla, and David R. Green. 2017.
719 Application of Structure-from-Motion Photogrammetry to River Restoration. Earth Sur-
720 face Processes and Landforms 42 (3): 503–15. doi:10.1002/esp.4086.
721 Micheletti, Natan, Christophe Lambiel, and Stuart N. Lane. 2015. Investigating Decadal-Scale
722 Geomorphic Dynamics in an Alpine Mountain Setting. Journal of Geophysical Research:
723 Earth Surface 120 (10): 2155–75. doi:10.1002/2015JF003656.
724 Milan, D.J., Heritage, G.L., Hetherington, D., 2007. Application of a 3D laser scanner in the as-
725 sessment of erosion and deposition volumes and channel change in a proglacial river.
726 Earth Surface Processes and Landforms 32 (11), 1657–1674.
727 Mondini, A. C., F. Guzzetti, P. Reichenbach, M. Rossi, M. Cardinali, and F. Ardizzone. 2011.
728 Semi-Automatic Recognition and Mapping of Rainfall Induced Shallow Landslides Us-
729 ing Optical Satellite Images. Remote Sensing of Environment 115 (7): 1743–57.
730 doi:10.1016/j.rse.2011.03.006.
731 Mondini, Alessandro C. 2017. Measures of Spatial Autocorrelation Changes in Multitemporal
732 SAR Images for Event Landslides Detection. Remote Sensing 9 (6): 554.
733 doi:10.3390/rs9060554.
734 Mondini, Alessandro Cesare, Fausto Guzzetti, Kang-Tsung Chang, Oriol Monserrat, Tapas Ran-
735 jan Martha, and Andrea Manconi. 2021. Landslide Failures Detection and Mapping Us-
736 ing Synthetic Aperture Radar: Past, Present and Future. Earth-Science Reviews 216
737 (May): 103574. doi:10.1016/j.earscirev.2021.103574.
738 Monti-Guarnieri, Andrea Virgilio, Maria Antonia Brovelli, Marco Manzoni, Mauro Mariotti
739 d'Alessandro, Monia Elisa Molinari, and Daniele Oxoli. 2018. Coherent Change Detec-
740 tion for Multipass SAR. IEEE Transactions on Geoscience and Remote Sensing 56 (11):
741 6811–22. doi:10.1109/TGRS.2018.2843560.

742 Mueller, Erich R., and John Pitlick. 2013. Sediment Supply and Channel Morphology in Moun-
743 tain River Systems: 1. Relative Importance of Lithology, Topography, and Climate. Jour-
744 nal of Geophysical Research: Earth Surface 118 (4): 2325–42.
745 doi:10.1002/2013JF002843.
746 Nagler, Thomas, Helmut Rott, Elisabeth Ripper, Gabriele Bippus, and Markus Hetzenecker.
747 2016. Advancements for Snowmelt Monitoring by Means of Sentinel-1 SAR. Remote
748 Sensing 8 (4): 348. doi:10.3390/rs8040348.
749 Olen S. and Bookhagen B. 2020. Applications of SAR Interferometric Coherence Time Series:
750 Spatiotemporal Dynamics of Geomorphic Transitions in the South-Central Andes. Jour-
751 nal of Geophysical Research: Earth Surface 125 (3): e2019JF005141.
752 doi:10.1029/2019JF005141.
753 Olen S., and Bookhagen B. 2018. Mapping Damage-Affected Areas after Natural Hazard Events
754 Using Sentinel-1 Coherence Time Series. Remote Sensing 10 (8): 1272.
755 doi: https://doi.org/10.3390/rs10081272
756 Passalacqua P., Dennis P.D., Jeffrey M.S., Simley D., Arrowsmith J.R., Bode C.A., Crosby C.,
757 DeLong S.B., Glenn N.F., Kelly S.A., Lague D., Sangireddt H., Schaffrath K., Tarboton
758 D.G., Wasklewicz T., Wheaton J.M., 2015. Analyzing high resolution topography for ad-
759 vancing the understanding of mass and energy transfer through landscapes: A review.
760 Earth Science Reviews 148: 174–193. DOI: 10.1016/j.earscirev.2015.05.012
761 Plank S. 2014. Rapid Damage Assessment by Means of Multi-Temporal SAR — A Comprehen-
762 sive Review and Outlook to Sentinel-1. Remote Sensing 6 (6): 4870–4906.
763 doi:10.3390/rs6064870.
764 https://www.planet.com. Last access 2/11/2022.
765 Prati, C., A. Ferretti, and D. Perissin. 2010. Recent Advances on Surface Ground Deformation
766 Measurement by Means of Repeated Space-Borne SAR Observations. Journal of Geody-
767 namics, WEGENER 2008 - Proceedings of the 14th General Assembly of Wegener, 49
768 (3): 161–70. doi:10.1016/j.jog.2009.10.011.
769 Purinton, Benjamin, and Bodo Bookhagen. 2020. Multiband (X, C, L) Radar Amplitude Analysis
770 for a Mixed Sand- and Gravel-Bed River in the Eastern Central Andes. Remote Sensing
771 of Environment 246 (September): 111799. doi:10.1016/j.rse.2020.111799.

Ravazzani, Giovanni, Secondo Barbero, Alessio Salandin, Alfonso Senatore, and Marco Mancini. 2015. An Integrated Hydrological Model for Assessing Climate Change Impacts on Water Resources of the Upper Po River Basin. Water Resources Management 29 (4): 1193–1215. doi:10.1007/s11269-014-0868-8.

Rawat, Kishan Singh, Vinay Kumar Sehgal, Sanatan Pradhan, and Shibendu S. Ray. 2017. Retrieval and Validation of Soil Moisture from FRS-1 Data Set of Radar Imaging Satellite (RISAT-1). Arabian Journal of Geosciences 10 (20): 445. doi:10.1007/s12517-017-3195-6.

Rosen, P.A., S. Hensley, I.R. Joughin, F.K. Li, S.N. Madsen, E. Rodriguez, and R.M. Goldstein. 2000. Synthetic Aperture Radar Interferometry. Proceedings of the IEEE 88 (3): 333–82. doi:10.1109/5.838084.

Rossi D., Zolezzi G., Bertoldi W., Vitti A. Monitoring Braided River-Bed Dynamics at the Sub-Event Time Scale Using Time Series of Sentinel-1 SAR Imagery. 2023. Remote Sensing 15(14), 3622; https://doi.org/10.3390/rs15143622

Rumsby, B. T., J. Brasington, J. A. Langham, S. J. McLelland, R. Middleton, and G. Rollinson. 2008. Monitoring and Modelling Particle and Reach-Scale Morphological Change in Gravel-Bed Rivers: Applications and Challenges. Geomorphology, Challenges in Geomorphological Methods and Techniques, 93 (1): 40–54. doi:10.1016/j.geomorph.2006.12.017.

Sanz-Ablanedo, E., Chandler, J.H., Ballesteros-Pérez, P., Rodriguez-Pérez, J.R., 2020. Reducing systematic dome errors in digital elevation models through better UAV flight design. Earth Surf. Process. Landforms 45, 2134–2147. https://doi.org/10.1002/esp. 4871.

Schaffrath, Keelin R., Patrick Belmont, and Joseph M. Wheaton. 2015. Landscape-Scale Geomorphic Change Detection: Quantifying Spatially Variable Uncertainty and Circumventing Legacy Data Issues. Geomorphology 250 (December): 334–48. doi:10.1016/j.geomorph.2015.09.020.

Schlaffer, Stefan, Marco Chini, Laura Giustarini, and Patrick Matgen. 2017. Probabilistic Mapping of Flood-Induced Backscatter Changes in SAR Time Series. International Journal of Applied Earth Observation and Geoinformation 56 (April): 77–87. doi:10.1016/j.jag.2016.12.003.

Schumann, G. J. P. 2021. The Full Potential of EO for Flood Applications: Managing Expectations. Earth Observation for Flood Applications, Elsevier, 305–320. doi.org/10.1016/B978-0-12- 819412-6.00014-6.

Schumann, G. J. P. 2019. The need for scientific rigour and accountability in flood mapping to better support disaster response, Hydrol. Process., 33, 3138–3142. doi.org/10.1002/hyp.13547, 2019.

Schumm S.A. and Lichty R.W. Time, space, and causality in geomorphology. American Journal of Science, Vol. 263, February 1965. P. 110-119. U.S. Geological Survey, Denver, Colorado

Sivasankar, Thota, Swakangkha Ghosh, and Mayank Joshi. 2021. Exploitation of Optical and SAR Amplitude Imagery for Landslide Identification: A Case Study from Sikkim, Northeast India. Environmental Monitoring and Assessment 193 (7): 386. doi:10.1007/s10661-021-09119-6.

TM-19_ptA.Pdf. 2019. Accessed January 28. https://www.esa.int/esapub/tm/tm19/TM-19_ptA.pdf.

Strick R.J.P., Ashworth P. J., Sambrook Smith G. H., Nicholas A. P., Best J. L., Lane S. N., Parsons D. R., Simpson C. J., Unsworth C. A., Dale J.. 2018. Quantification of bedform dynamics and bedload sediment flux in sandy braided rivers from airborne and satellite imagery. Earth Surface Processes and Landforms. https://doi.org/10.1002/esp.4558

Tarpanelli A., Mondini A.C. and Camici S. 2022. Effectiveness of Sentinel-1 and Sentinel-2 for flood detection assessment in Europe. Natural Hazards Earth System Sciences, 22, 2473–2489. doi.org/10.5194/nhess-22-2473-2022

Ullmann T., Büdel C., Baumhauer R., and Padashi M. 2016. Sentinel-1 SAR Data Revealing Fluvial Morphodynamics in Damghan (Iran): Amplitude and Coherence Change Detection. International Journal of Earth Science and Geophysics 2 (1). doi:10.35840/2631-5033/1807.

Wallace, Luke, Arko Lucieer, Zbyněk Malenovský, Darren Turner, and Petr Vopěnka. 2016. Assessment of Forest Structure Using Two UAV Techniques: A Comparison of Airborne Laser Scanning and Structure from Motion (SfM) Point Clouds. Forests 7 (3): 62. doi:10.3390/f7030062.

Walter, T. R., M. Shirzaei, A. Manconi, G. Solaro, A. Pepe, M. Manzo, and E. Sansosti. 2014. Possible Coupling of Campi Flegrei and Vesuvius as Revealed by InSAR Time Series, Correlation Analysis and Time Dependent Modeling. Journal of Volcanology and Geothermal Research 280 (June): 104–10. doi:10.1016/j.jvolgeores.2014.05.006.

Westaway, R. M., S. N. Lane, and D. M. Hicks. 2000. The development of an automated correction procedure for digital photogrammetry for the study of wide, shallow, gravel-bed rivers. Earth Surface Processes and Landforms 25 (2): 209–26. doi:10.1002/(SICI)1096-9837(200002)25:2<209::AID-ESP84>3.0.CO;2-Z.

Wheaton, J. M., Brasington J., Darby S.E., Kasprak A., Sear D., and Vericat D. 2013. Morphodynamic Signatures of Braiding Mechanisms as Expressed through Change in Sediment Storage in a Gravel-Bed River: MORPHODYNAMIC SIGNATURES OF BRAIDING. Journal of Geophysical Research: Earth Surface 118 (2): 759–79. doi:10.1002/jgrf.20060.

Wheaton, Joseph M., James Brasington, Stephen E. Darby, and David A. Sear. 2010. Accounting for uncertainty in DEMs from repeat topographic surveys: improved sediment budgets. Earth Surface Processes and Landforms 35 (2): 136–56. doi:10.1002/esp.1886.

Williams, R. D., C. D. Rennie, J. Brasington, D. M. Hicks, and D. Vericat. 2015. Linking the Spatial Distribution of Bed Load Transport to Morphological Change during High-Flow Events in a Shallow Braided River: Spatially Distributed Bedload Transport. Journal of Geophysical Research: Earth Surface 120 (3): 604–22. doi:10.1002/2014JF003346.

852

Tabella 1. Area, Ground resolution, Root Mean Square Error (RMSE) (along X - Longitude, Y – Latitude and Z – Altitude) and STandard DEViation (STDEV) along the z direction for both Control Points (GCP) and Check Points (CP). The GCPs used for the two acquisitions are reported between parentheses in the RMSEtot column.

			GCPs			
Year	Area (km^2)	Ground resolution (cm/pixel)	RMSE tot (cm)	RMSE xy (cm)	RMSE z (cm)	STDEV z (cm)
2017	0.16	2.09	(6) 3.35	3.08	1.32	1.38
2018	0.34	2.04	(14) 4.32	3.19	2.91	2.65
			CPs			
2017	0.16	2.09	(3) 6.58	6.20	2.21	2.22
2018	0.34	2.04	(6) 5.01	3.75	3.32	3.26

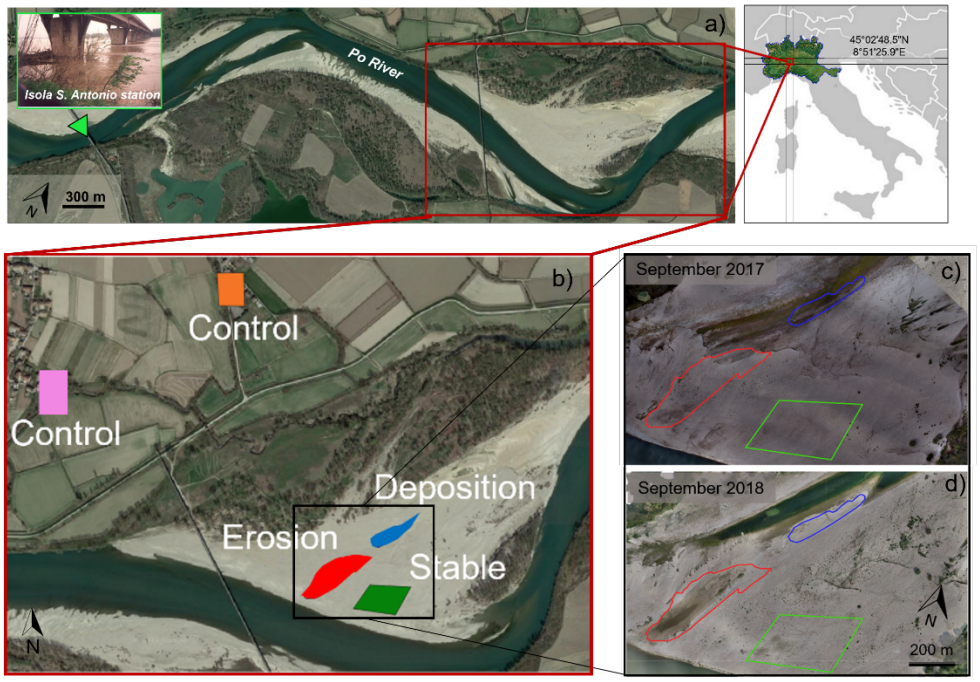

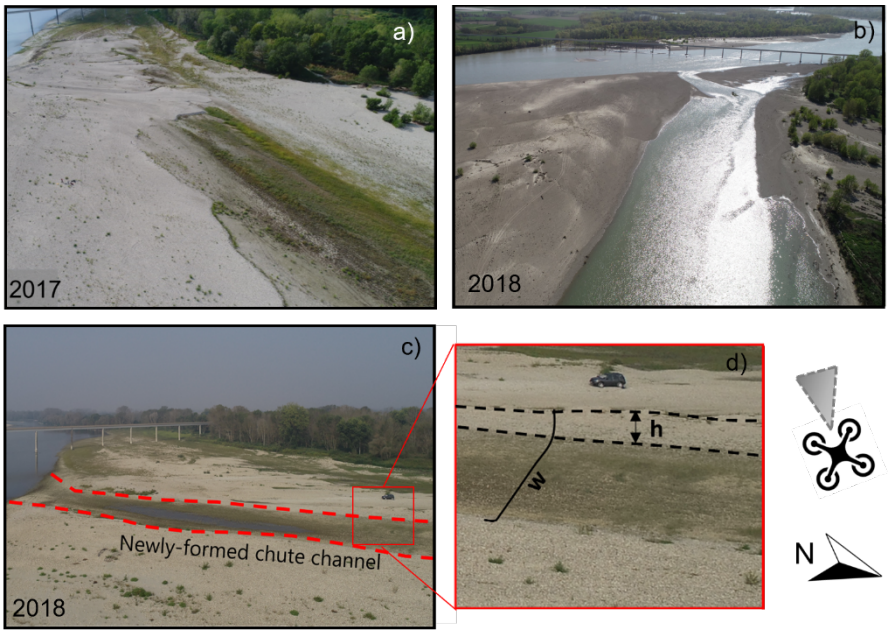

861

862

863

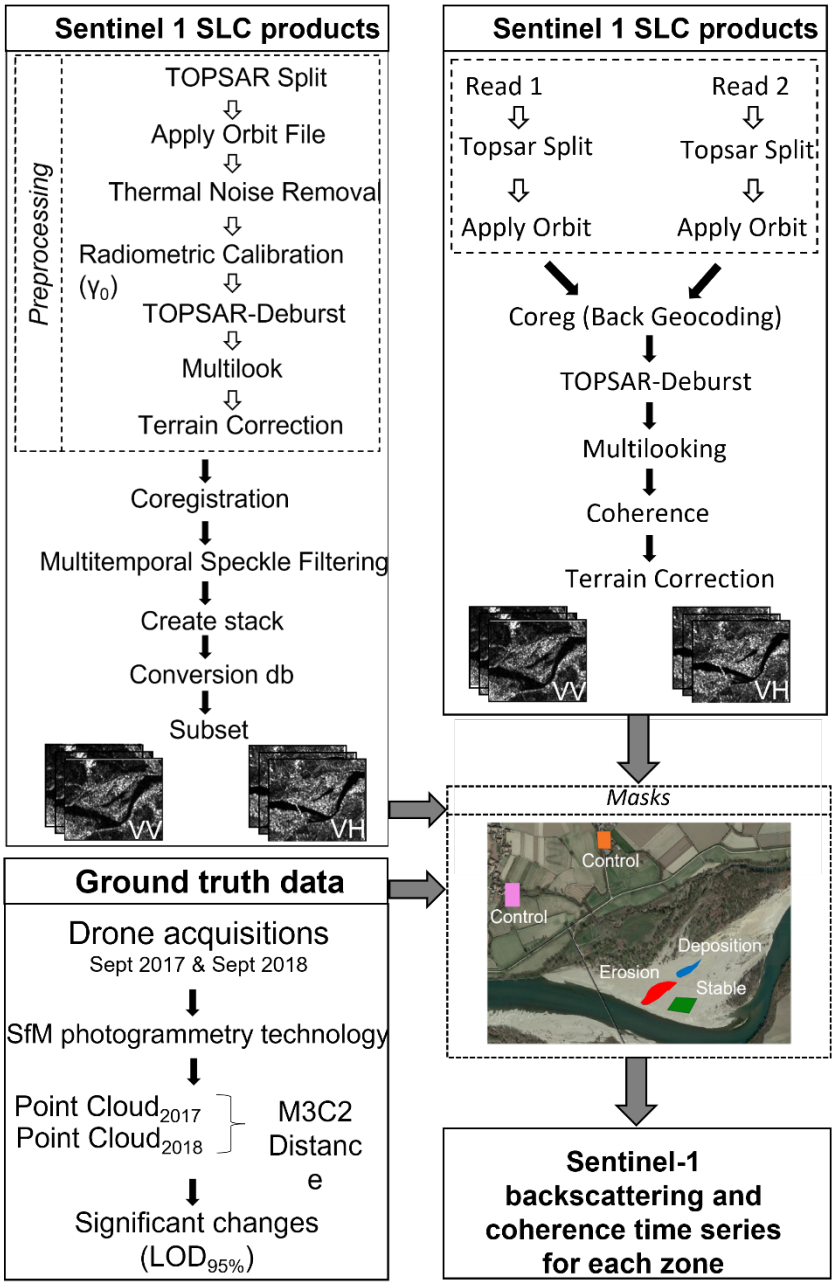
Sentinel 1 SLC products
Preprocessing
TOPSAR Split
Apply Orbit File
Thermal Noise Removal
Radiometric Calibration
(γ_0)
TOPSAR-Deburst
Multilook
Terrain Correction
Coregistration
Multitemporal Speckle Filtering
Create stack
Conversion db
Subset
VV
VH
Sentinel 1 SLC products
Read 1
Read 2
Topsar Split
Topsar Split
Apply Orbit
Apply Orbit
Coreg (Back Geocoding)
TOPSAR-Deburst
Multilooking
Coherence
Terrain Correction
VV
VH
Masks
Control
Control
Deposition
Erosion
Stable
Ground truth data
Drone acquisitions
Sept 2017 & Sept 2018
SfM photogrammetry technology
Point Cloud$_{2017}$
Point Cloud$_{2018}$
M3C2 Distance
Significant changes
(LOD$_{95\%}$)
Sentinel-1 backscattering and coherence time series for each zone

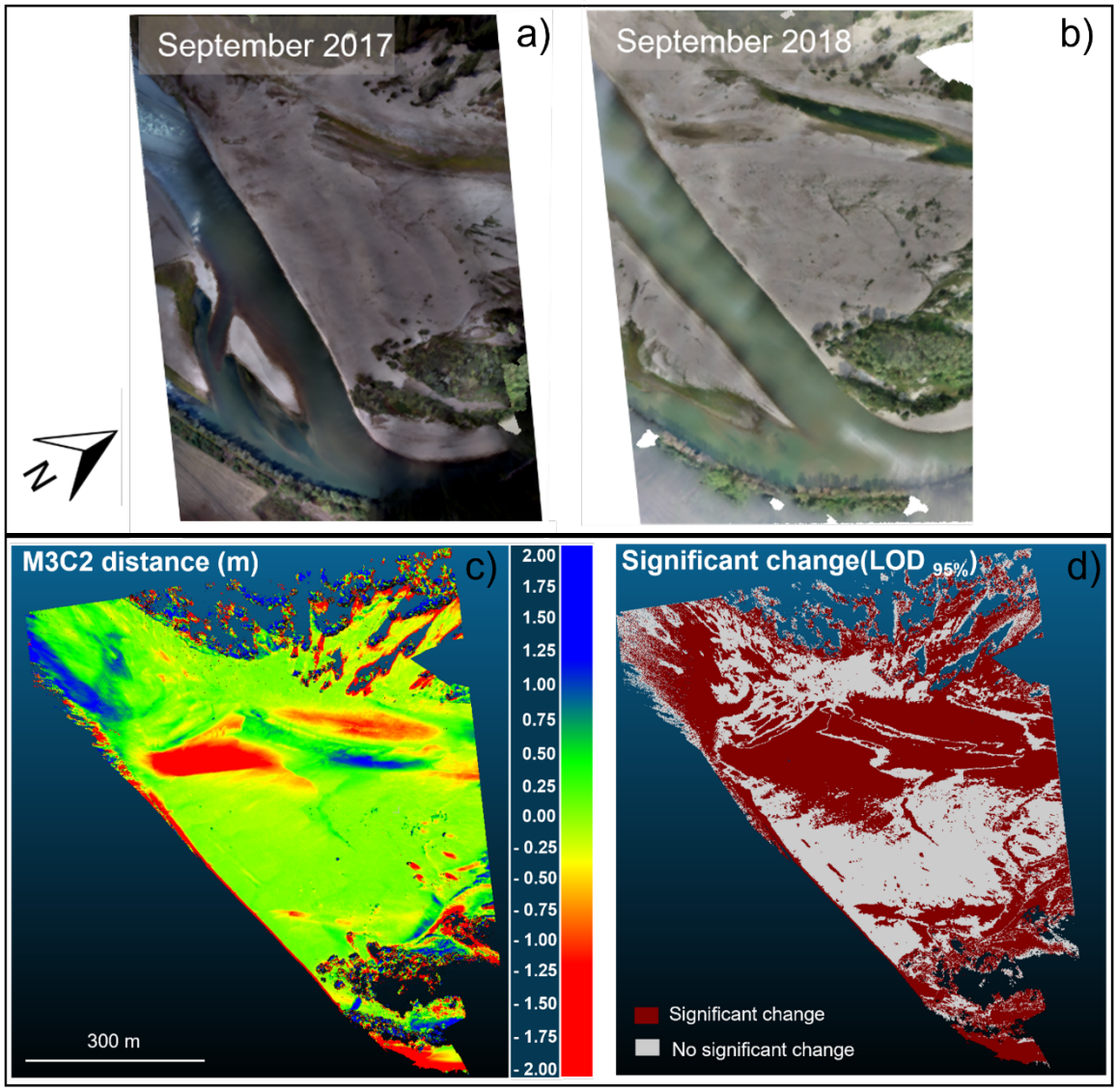
September 2017
a)
September 2018
b)
N
M3C2 distance (m)
c)
2.00
1.75
1.50
1.25
1.00
0.75
0.50
0.25
0.00
- 0.25
- 0.50
- 0.75
- 1.00
- 1.25
- 1.50
- 1.75
- 2.00
300 m
Significant change(LOD 95%)
d)
Significant change
No significant change

864

865

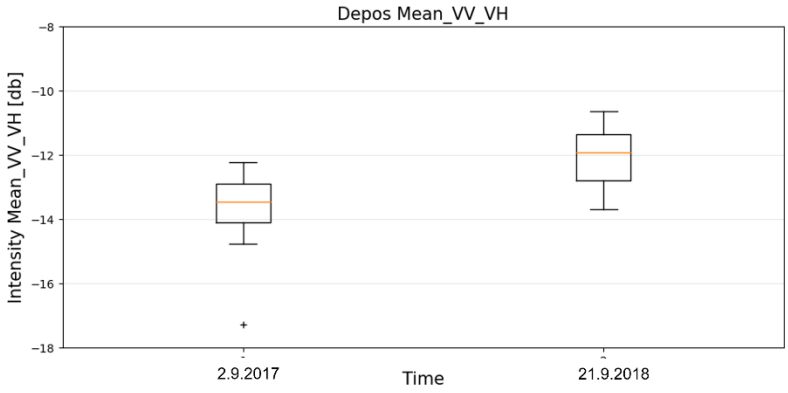
Depos Mean_VV_VH
Intensity Mean_VV_VH [db]
−8
−10
−12
−14
−16
−18
2.9.2017
Time
21.9.2018

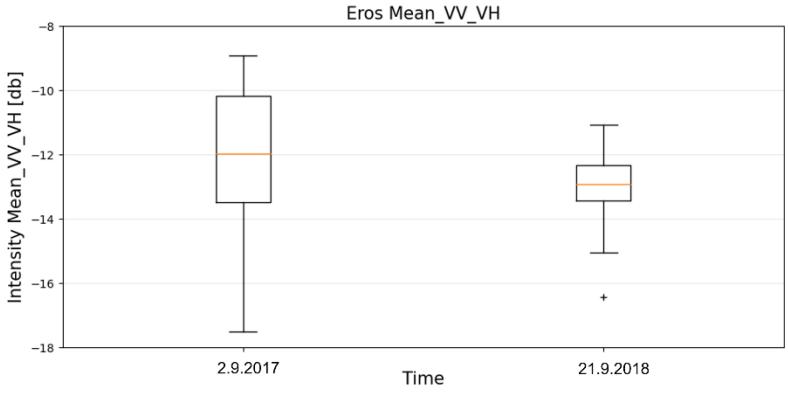
Eros Mean_VV_VH
Intensity Mean_VV_VH [db]
−8
−10
−12
−14
−16
−18
2.9.2017
Time
21.9.2018

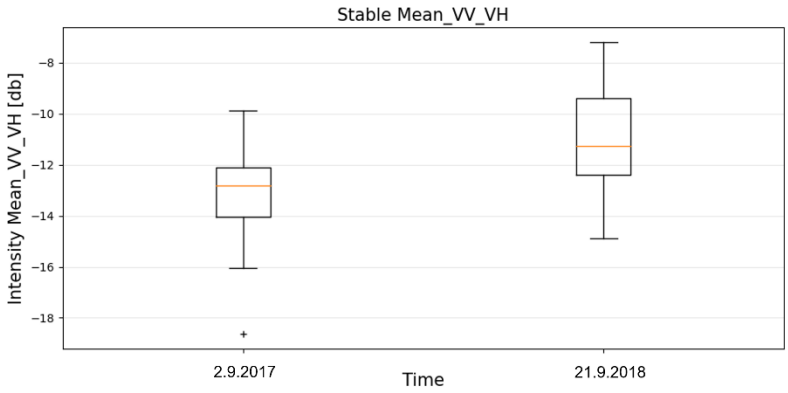
Stable Mean_VV_VH
Intensity Mean_VV_VH [db]
−8
−10
−12
−14
−16
−18
2.9.2017
Time
21.9.2018

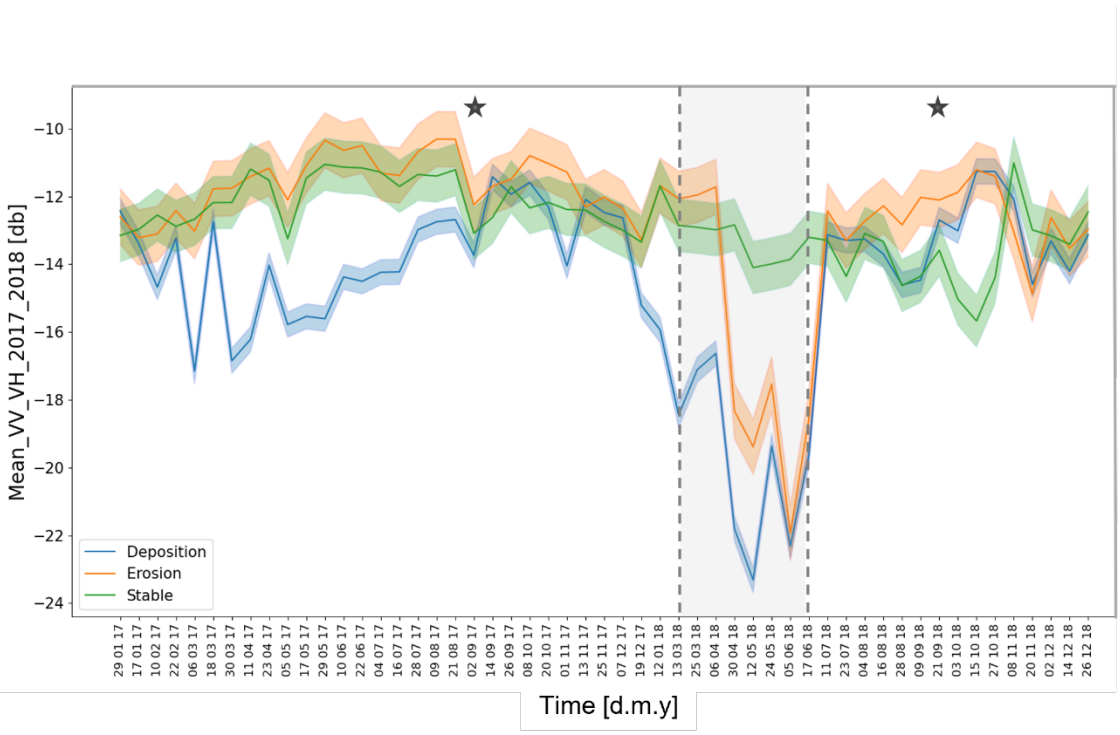
Mean_VV_VH_2017_2018 [db]
−10
−12
−14
−16
−18
−20
−22
−24
Deposition
Erosion
Stable
29 01 17
17 01 17
10 02 17
22 02 17
06 03 17
18 03 17
30 03 17
11 04 17
23 04 17
05 05 17
17 05 17
29 05 17
10 06 17
22 06 17
04 07 17
16 07 17
28 07 17
09 08 17
21 08 17
02 09 17
14 09 17
26 09 17
08 10 17
20 10 17
01 11 17
13 11 17
25 11 17
07 12 17
19 12 17
12 01 18
13 03 18
25 03 18
06 04 18
30 04 18
12 05 18
24 05 18
05 06 18
17 06 18
11 07 18
23 07 18
04 08 18
16 08 18
28 08 18
09 09 18
21 09 18
03 10 18
15 10 18
27 10 18
08 11 18
20 11 18
02 12 18
14 12 18
26 12 18
Time [d.m.y]

867

868

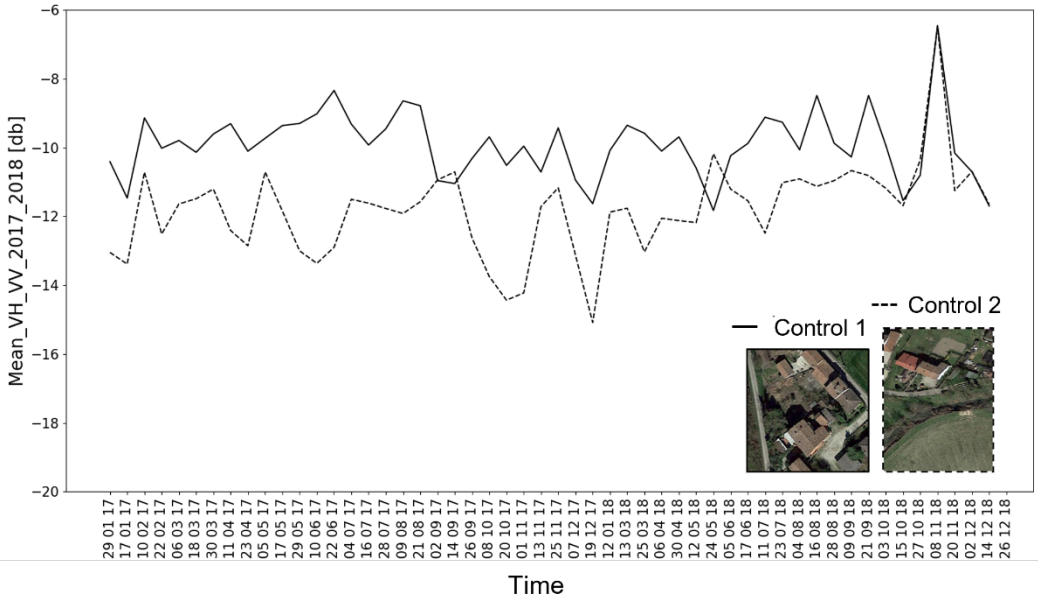
Mean_VH_VV_2017_2018 [db]
−6
−8
−10
−12
−14
−16
−18
−20
Control 1
Control 2
Time

869

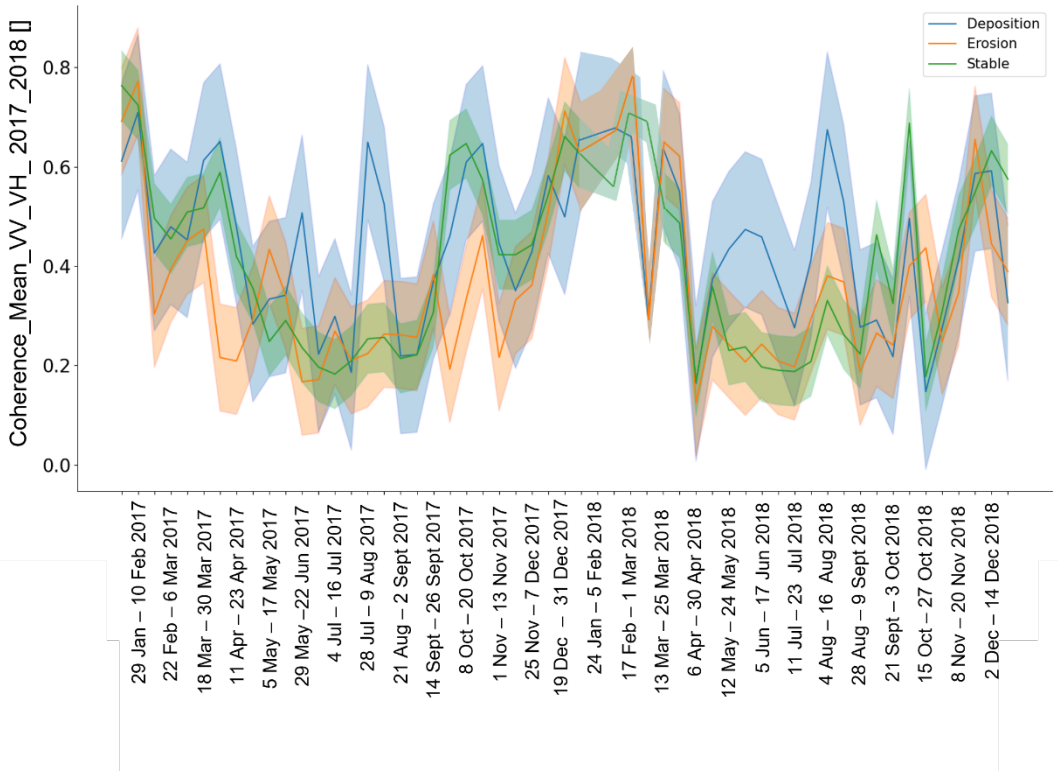
Coherence_Mean_VV_VH_ 2017_2018 []
0.0
0.2
0.4
0.6
0.8
Deposition
Erosion
Stable
29 Jan – 10 Feb 2017
22 Feb – 6 Mar 2017
18 Mar – 30 Mar 2017
11 Apr – 23 Apr 2017
5 May – 17 May 2017
29 May –22 Jun 2017
4 Jul – 16 Jul 2017
28 Jul – 9 Aug 2017
21 Aug – 2 Sept 2017
14 Sept – 26 Sept 2017
8 Oct – 20 Oct 2017
1 Nov – 13 Nov 2017
25 Nov – 7 Dec 2017
19 Dec – 31 Dec 2017
24 Jan – 5 Feb 2018
17 Feb – 1 Mar 2018
13 Mar – 25 Mar 2018
6 Apr – 30 Apr 2018
12 May – 24 May 2018
5 Jun – 17 Jun 2018
11 Jul – 23 Jul 2018
4 Aug – 16 Aug 2018
28 Aug – 9 Sept 2018
21 Sept – 3 Oct 2018
15 Oct – 27 Oct 2018
8 Nov – 20 Nov 2018
2 Dec – 14 Dec 2018

870

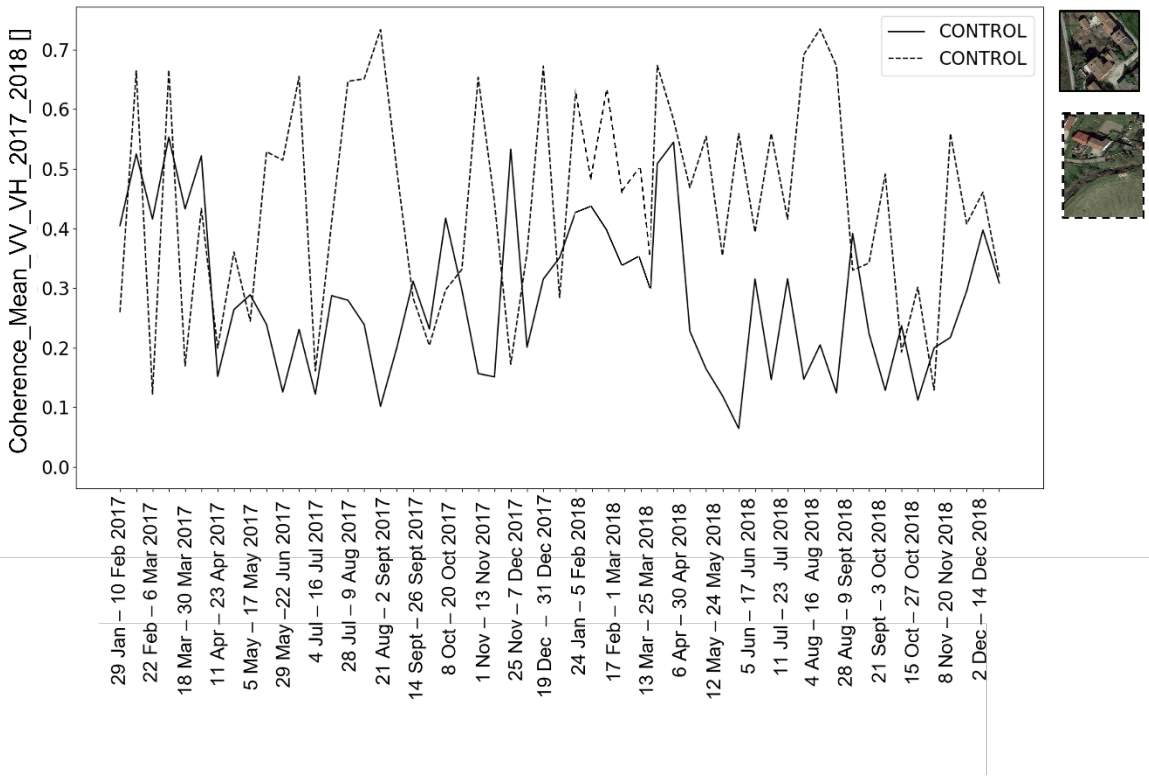
Coherence_Mean_VV_VH_2017_2018 []
0.0
0.1
0.2
0.3
0.4
0.5
0.6
0.7
CONTROL
CONTROL
29 Jan – 10 Feb 2017
22 Feb – 6 Mar 2017
18 Mar – 30 Mar 2017
11 Apr – 23 Apr 2017
5 May – 17 May 2017
29 May –22 Jun 2017
4 Jul – 16 Jul 2017
28 Jul – 9 Aug 2017
21 Aug – 2 Sept 2017
14 Sept – 26 Sept 2017
8 Oct – 20 Oct 2017
1 Nov – 13 Nov 2017
25 Nov – 7 Dec 2017
19 Dec – 31 Dec 2017
24 Jan – 5 Feb 2018
17 Feb – 1 Mar 2018
13 Mar – 25 Mar 2018
6 Apr – 30 Apr 2018
12 May – 24 May 2018
5 Jun – 17 Jun 2018
11 Jul – 23 Jul 2018
4 Aug – 16 Aug 2018
28 Aug – 9 Sept 2018
21 Sept – 3 Oct 2018
15 Oct – 27 Oct 2018
8 Nov – 20 Nov 2018
2 Dec – 14 Dec 2018

871

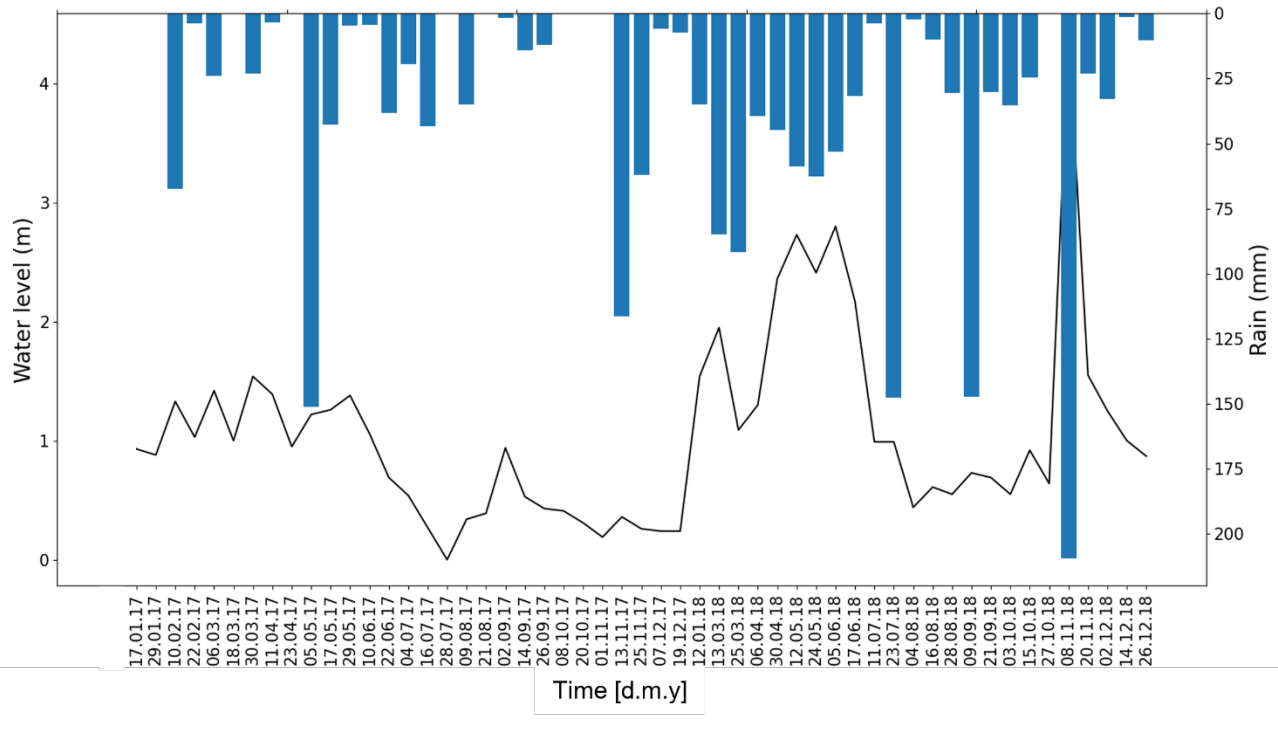
Water level (m)
0
1
2
3
4
Rain (mm)
0
25
50
75
100
125
150
175
200
17.01.17
29.01.17
10.02.17
22.02.17
06.03.17
18.03.17
30.03.17
11.04.17
23.04.17
05.05.17
17.05.17
29.05.17
10.06.17
22.06.17
04.07.17
16.07.17
28.07.17
09.08.17
21.08.17
02.09.17
14.09.17
26.09.17
08.10.17
20.10.17
01.11.17
13.11.17
25.11.17
07.12.17
19.12.17
12.01.18
13.03.18
25.03.18
06.04.18
30.04.18
12.05.18
24.05.18
05.06.18
17.06.18
11.07.18
23.07.18
04.08.18
16.08.18
28.08.18
09.09.18
21.09.18
03.10.18
15.10.18
27.10.18
08.11.18
20.11.18
02.12.18
14.12.18
26.12.18
Time [d.m.y]

872


Sept 2017
206.4 m³/s
Jan 2018
358.4 m³/s
Apr 2018
748.2 m³/s
May 2018
1183.8 m³/s
Jun 2018
946.96 m³/s
Jun 2018
328.5 m³/s
Aug 2018
N
400 m
194.6 m³/s
Sept 2018
242.9 m³/s
Dec 2018
322.7 m³/s

873

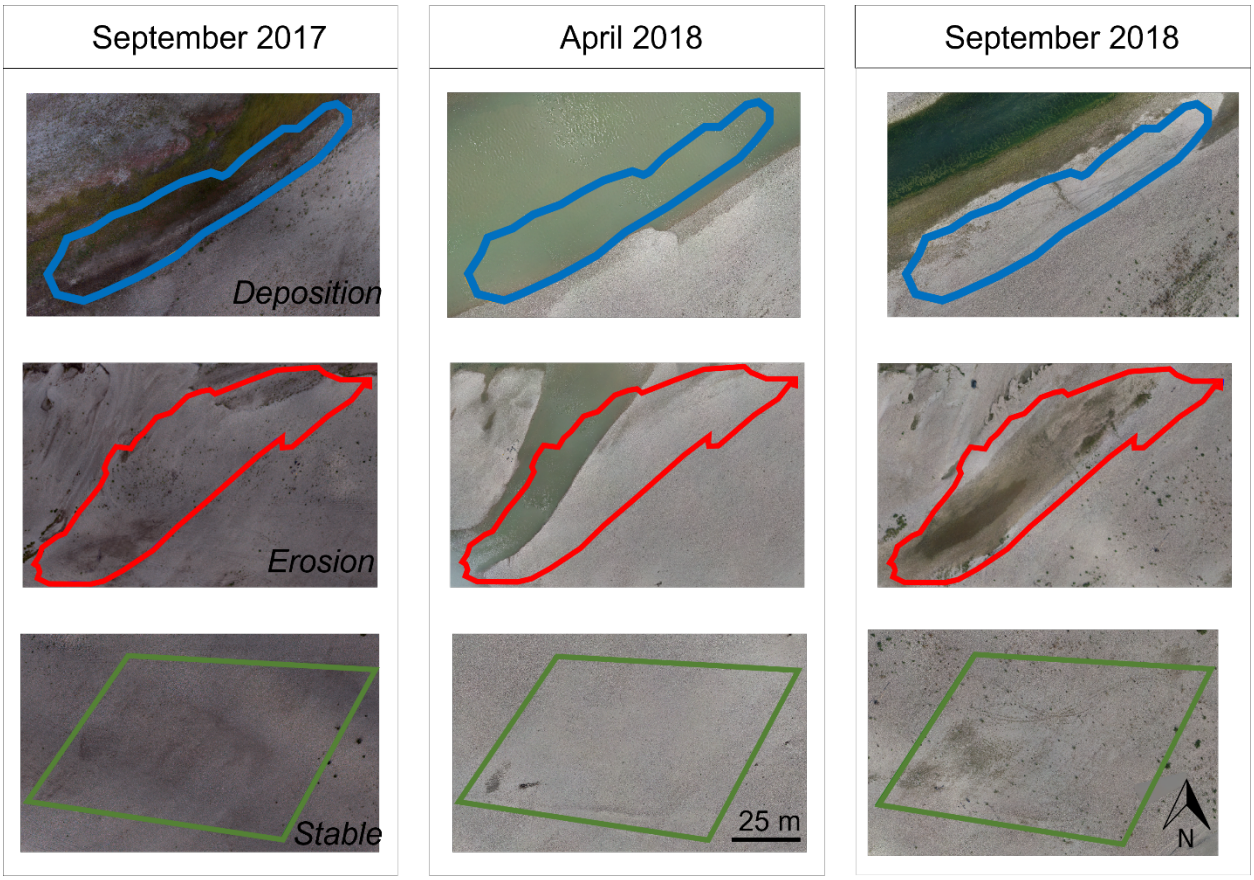

Figure 1. Study area: the location of the sediment bar along the Po River (highlighted by a red square) and the correspondent coordinates and the location of the hydro-meteorological station named Isola S. Antonio (a); The river bar under study taken from orthophoto from drone images, in September 2017 and September 2018. A zoom on the study site (b) from google satellite image, with top the polygons delineating the areas ('Erosion', 'Deposition', 'Stable', 'Control') later used as masks for the correlation analysis with the radar derived data. A zoom on the ortophotos (c) acquired in September 2017 and September 2018, with top the polygons delineating the 3 areas ('Erosion', 'Deposition'. 'Stable').

Figure 2. UAV images collected in September 2017 (a), April 2018 (b), September 2018 (c) at about 60 m altitude on the diagonal bar selected as study site; a zoom of the eroded channel (d) gives insights about the condition of the secondary eroded channel and its geometric features: channel width accounts for about 30 m, channel height is in the range of 1.5 - 2 m deep, as can be

888 seen from the comparison with the height of the car present in the site (Land Rover defender model,
889 height of about 2 m).

890 Figure 3. Schematic representation of the workflow followed for Sentinel-1 backscattering data
891 extraction in each zone. The preprocessing of Sentinel-1 SLC products was conducted in SNAP,
892 to obtain VV and VH polarizations. Drone acquisitions were used to generate 3D point cloud and
893 calculate the significant distance among the two clouds via the M3C2 plugin available in
894 CloudCompare software, for morphological changes identification. A mask on the areas identified
895 was applied to the Sentinel-1 images, to extract pixels belonging to each zone.

896 Figure 4. Ortophotos generated at 10 cm resolution from the UAV acquisitions conducted in
897 September 2017 (a) and September 2018 (b). Distance map expressed in terms of meters (c),
898 resulting from the distance computation between the point clouds of the two acquisitions (2017
899 and 2018), estimated with the M3C2 algorithm in CloudCompare. Significance (95% confidence
900 level) map of the estimated changes (d).

901 Figure 5. Boxplot of the intensity values (expressed as mean of VV and VH polarization) of the
902 three zones pre and post the flood event, respectively in September 2017 and September 2018
903 (close to the ground truth dataset acquisitions). Despite in 2017-2018 there are some differences,
904 they are lower or within the range of. within the expected errors of the analysis performed (± 5
905 dB). Therefore, it is not possible to discriminate changes associated to other factors than noise.

906 Figure 6: decider se mettere quella con spatial distribution of intensity values

907 Figure 6/7. Time series of intensity values of Sentinel-1 registered in the 3 zones characterized by
908 different morphological changes - erosion, deposition and stable. On the x axes dates selected
909 throughout the years; on the y axes the mean backscattering value of all pixels belonging to each
910 zone, expressed in dB, calculated as the mean of VV and VH polarizations. Gray dashed lines
911 indicate dates where the bar was inundated. Dark gray stars indicate the same dates analyzed in
912 figure 6. No specific trends are visible for erosional/depositional processes in comparison to the
913 stable area through most of the time, except from March to late June 2018 when the high-water
914 level remained considerably high, and a great portion of the sediment bar was inundated.

915 Figure 7/8. Plot of the intensity values of the 'Control' areas selected as reference outside the study
916 site. These areas are composed of mixed land cover (buildings, trees, fields, roads). On the x axes

dates selected throughout the years; on the y axes the mean backscattering value of all pixels belonging to each zone, expressed in dB, calculated as the mean of VV and VH polarizations.

Figure 8/9. Time series of coherence values of Sentinel-1 registered in the 3 zones characterized by different morphological changes - erosion, deposition and stable. On the x axes the dates of the image pairs selected throughout the years from January 2017 to December 2018; on the y axes the mean coherence value of all pixels belonging to each zone, calculated as the mean of VV and VH polarizations for each image pair.

Figure 9/10. Plot of the coherence values of the 'Control' areas selected as reference outside the study site. These areas are composed of mixed land cover (buildings, trees, fields, roads). On the x axes dates selected throughout the years; on the y axes the mean coherence value of all pixels belonging to each zone calculated as the mean of VV and VH polarizations.

Figure 10/11. Rainfall and water level data registered by the Isola Sant'Antonio hydro-meteorological station.

Figure 11/12. Planet RGB satellite images on the sediment bar, selected in specific dates representative of the period investigated.

Figure 12/13. Zoom on the ortophotos, generated from the UAV acquisitions made in September 2017, April 2018, September 2018, of the three zones identified interested as 'Erosion', 'Deposition', 'Stable'.